

Internal layers in turbulent free-shear flowsD. Fiscaletti ^{*}*Department of Aerodynamics, Wind Energy and Propulsion, Delft University of Technology,
Kluyverweg 1, 2629 HS Delft, The Netherlands*O. R. H. Buxton[†]*Department of Aeronautics, Imperial College London, London SW7 2AZ, England, United Kingdom*A. Attili[‡]*Institute for Multiscale Thermo fluids, School of Engineering, University of Edinburgh,
Edinburgh EH9 3FD, Scotland, United Kingdom*

(Received 17 September 2020; accepted 4 March 2021; published 17 March 2021)

The characteristics of the internal layers of intense shear are examined in a mixing layer and in a jet, in the range of Reynolds numbers $134 < \text{Re}_\lambda < 275$. Conditionally averaged profiles of streamwise velocity conditioned on the identified internal layers present strong velocity jumps, which account for approximately 10% of the characteristic large-scale velocity of the flow. The thickness $\langle \delta_w \rangle$ of the internal layers from the combined analysis of both the mixing layer and the jet scales with $\langle \delta_w \rangle / \lambda \sim \text{Re}_\lambda^{-1/2}$, which suggests a scaling with the Kolmogorov length scale (η), analogous to recent observations on the turbulent/nonturbulent interface (TNTI). The thickness of the internal shear layers within the mixing layer is found to be between 9η and 11η . The concentration of a passive scalar across the internal layers is also examined, at the Schmidt number $\text{Sc} = 1.4$. The scalar concentration does not show any jumps across the internal layers, which is an important difference between the internal layers and the TNTI. This can be explained from the analysis of the internal layers of intense scalar gradient, where the flow topology node/saddle/saddle dominates, associated with strain, whereas the internal layers of intense shear are characterized by a prevalence of focus/stretching. A topological content analogous to that obtained in layers of intense scalar gradient is found in proximity to the TNTI, at the boundary between the viscous superlayer and the turbulent sublayer. These observations evidence that the TNTI and the internal layers of intense scalar gradient are similar in several respects.

DOI: [10.1103/PhysRevFluids.6.034612](https://doi.org/10.1103/PhysRevFluids.6.034612)**I. INTRODUCTION**

In turbulent flows developing within a quiescent and/or nonturbulent environment, a convoluted and intermittent layer separates the turbulent region from the external fluid. Across this interfacial layer, turbulent entrainment of the external fluid occurs, and controls the transport of mass, momentum, and scalar from the nonturbulent region into the turbulent one. Turbulent transport and mixing are relevant to several engineering processes and natural phenomena, such as combustion, volcano

^{*}d.fiscaletti@delft.nl[†]o.buxton@imperial.ac.uk[‡]antonio.attili@ed.ac.uk

plumes, and extreme weather events. The turbulent/nonturbulent interface (TNTI) has therefore received increasing interest over the past two decades, after the pioneering work of Corrsin and Kistler [1] postulated the nature of this layer.

Several studies presented conditional averages of streamwise velocity, vorticity, and scalar concentration conditioned on the position within the TNTI (Bisset *et al.* [2], Westerweel *et al.* [3], Westerweel *et al.* [4], Gampert *et al.* [5], Gampert *et al.* [6], van Reeuwijk and Holzner [7], Attili *et al.* [8], Chauhan *et al.* [9]). These averages showed the existence of a steep jump of the aforementioned physical quantities across the TNTI of several different turbulent flows, both wall bounded and boundary free. The jump in the average profile of the streamwise velocity was found to govern the entrainment and the growth rate of these turbulent flows. Moreover, it has been an object of literature debate whether the entrainment of quiescent fluid is a small-scale process dominated by viscosity (nibbling) or a large-scale inviscid process (engulfment). The characteristics of the TNTI were therefore investigated to shed a light on this matter. According to a number of experimental and numerical investigations, the thickness of the TNTI is in the order of the Taylor microscale (Bisset *et al.* [2], Gampert *et al.* [5], Westerweel *et al.* [4], Chauhan *et al.* [10], Borrell and Jiménez [11]). However, following the recent works based on the analysis of flows at a large range of Reynolds numbers and at a high spatial resolution, this observation was reconsidered, and a Kolmogorov scaling was proposed (Silva *et al.* [12], Watanabe *et al.* [13], Watanabe *et al.* [14], Attili *et al.* [8]). Regardless, the TNTI was found to be a small-scale feature, which leads us to think of entrainment as a process dominated by viscosity, although Mistry *et al.* [15] showed that the mass-flux rate across the interface is constant across all the turbulence scales. This evidence suggests that the net entrainment is a scale-independent process, therefore it is not dominated by the viscous scales.

Recently, Eisma *et al.* [16] showed that layers of intense shear, somehow similar to the TNTI, exist within the internal region of a turbulent boundary layer. The entrainment velocity of these internal layers, defined as the velocity at which the internal layers move away from the wall in a Lagrangian sense, was estimated based on the large-scale properties of the conditionally averaged profiles of velocity and Reynolds stress. Later, de Silva *et al.* [17] and Fan *et al.* [18] examined the interfaces between adjacent zones of uniform momentum in a turbulent boundary layer. These studies showed that jumps in the streamwise velocity exist across internal layers, and scale with the friction velocity, while the thickness of these interfaces scales with the Taylor microscale. Gul *et al.* [19] experimentally investigated internal shear layers in a pipe flow, with time-resolved stereoscopic particle image velocimetry (PIV). Conditional averages across these layers revealed jumps of several flow properties, including turbulent shear stress, streamwise, and wall-normal velocities. Stronger velocity jumps were observed when moving progressively closer to the wall, and at increasing Reynolds number. Layers of intense shear were also reported in homogeneous isotropic turbulence at very high Reynolds numbers, both from statistical considerations (Elsinga *et al.* [20]) and instantaneous snapshots (Ishihara *et al.* [21], Hunt *et al.* [22]). The analysis of the average flow pattern in the local coordinate system defined by the eigenvectors of the strain rate tensor revealed a shear-layer structure consisting of aligned vortical motions (Elsinga and Marusic [23], Elsinga *et al.* [20]). A similar structure was also observed from instantaneous snapshots, where sharp layers of approximately four Taylor length scales in thickness were found to bound regions of different large-scale velocities (Ishihara *et al.* [21]). The existence of internal layers was so far ascertained in turbulent boundary layers and in homogeneous isotropic turbulence, whereas boundary-free-shear flows have never been examined. Moreover, although Attili *et al.* [8] and Gampert *et al.* [6] reported a jump across the TNTI of a mixing layer, the concentration of a passive scalar across the internal layers has never been analyzed.

The main goal of the present paper is to investigate the internal layers within a mixing layer and a jet, at a range of Reynolds numbers $134 < \text{Re}_\lambda < 275$. Profiles of velocity and scalar concentration at Schmidt numbers of the order of unity are examined across these layers, with the aim of determining their properties, with a particular focus on their thickness scaling and velocity jump. In the mixing layer, three different streamwise locations, corresponding to three different Reynolds numbers, are considered. The largest Reynolds number of the mixing layer under analysis

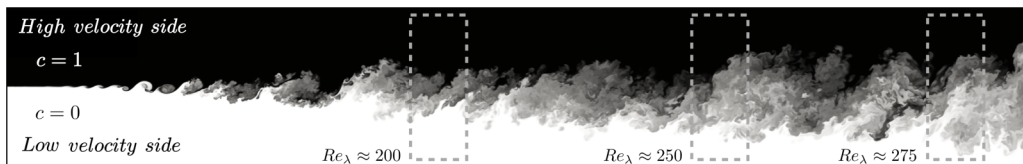


FIG. 1. Two-dimensional cut of the scalar field at Schmidt number 1.4 in the turbulent mixing layer obtained from direct numerical simulations. The three regions delimited by squares of thick dashed lines identify the three subdomains analyzed in the present paper.

is $Re_\lambda = 275$, and to the authors' best knowledge this is the largest ever achieved in direct numerical simulation (DNS) of this flow. The jet data are obtained from experiments of tomographic PIV at high spatial resolution. In the jet, the effect of the initial conditions on the characteristics of the internal layers is also examined. Specifically, we study the properties of the internal layers within a jet issuing from orifices of different geometries, i.e., a circular orifice and a fractal orifice, in order to ascertain the effects of the jet initial conditions on the internal layers.

In their work, Elsinga and da Silva [24] discuss analogies and dissimilarities between the TNTI and the internal layers. The internal layers are shear layers bounded by nearly uniform flow on both sides, which is analogous to the TNTI. However, while strain is prevalent over vorticity in the turbulent region of the TNTI, in the internal layers both strain and vorticity are significant. As a result, the scalar front is parallel to the TNTI, whereas it is at an angle of approximately 20° with respect to the internal layers. This explains the scalar jump observed at the TNTI (Gampert *et al.* [6], Attili *et al.* [8] among others) and the low scalar gradient in points of high vorticity (Brethouwer *et al.* [25]). Nonetheless, the properties and the spatial organization of the regions at intense scalar gradient have never been examined in relation to the internal layers of intense shear and to the TNTI. In the second part of the present paper, the flow topology of the regions at intense scalar gradient is examined, and compared with the topological content of the internal layers of intense shear, and of the TNTI. Conditionally averaged profiles of streamwise velocity are also computed across the identified regions of intense scalar gradient. Furthermore, the relative position of intense scalar gradient and of internal layers of intense shear is statistically examined.

II. METHODS

Two turbulent free-shear flows are analyzed in this paper, namely, a mixing layer from DNS and a jet from experiments. In the following, the datasets of both flows are illustrated, as well as the methods of analysis that are applied to them.

A. Mixing layer

The dataset employed in the present analysis was generated with a large-scale DNS of a high Reynolds number, spatially developing mixing layer, featuring a grid of about 18×10^9 points. The configuration and methods applied in these simulations are described in detail by Attili and Bisetti [26], Attili and Bisetti [27], and Attili *et al.* [8]. Analogous DNS datasets of a mixing layer were previously employed to investigate the interaction between the large and the small scales of turbulence (Fiscaletti *et al.* [28,29]). Compared to the simulations described in the cited papers, the Reynolds number of the turbulent flow that is analyzed here was increased up to $Re_\lambda \approx 275$. The spatial resolution of the numerical dataset is of approximately 2η . A two-dimensional cut of the scalar field at Schmidt number 1.4 in the turbulent mixing layer is shown in Fig. 1. Here, three regions delimited by squares of thick dashed lines identify the three subdomains analyzed in this paper, corresponding to three different Reynolds numbers, i.e., $Re_\lambda \approx 200$, 250, and 275. We note that the initial distribution of the scalar concentration is such that the top side of the mixing layer

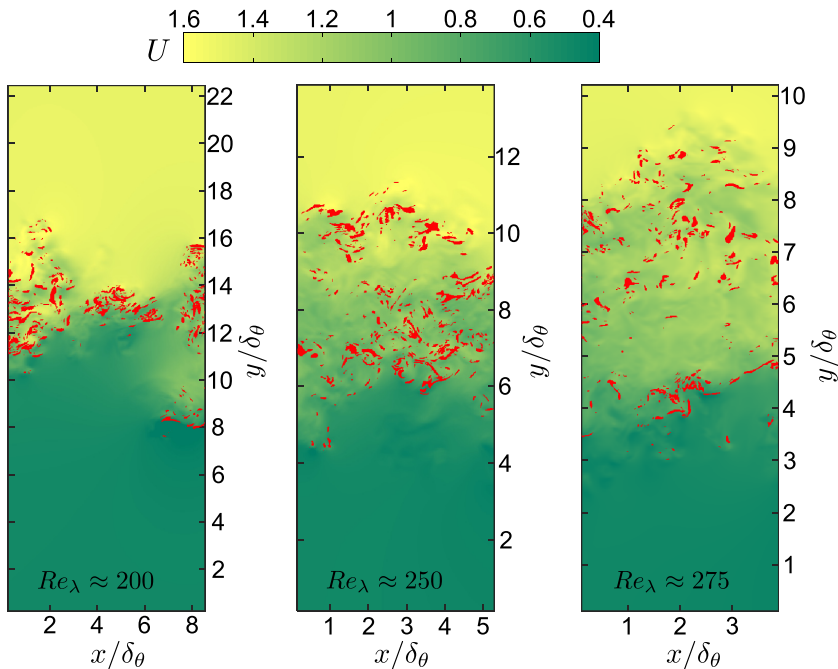


FIG. 2. Snapshots of the streamwise velocity at constant z within the mixing layer, obtained at the three different downstream locations shown in Fig. 1, corresponding to the three different Reynolds numbers $Re_\lambda \approx 200, 250,$ and 275 . The regions characterized by intense shear and obtained with $K = 1.5$ in Eq. (2) are shown in red. The streamwise and crosswise coordinates, respectively x and y , are nondimensionalized by the local momentum thickness δ_θ .

is characterized by 100% scalar concentration, while the bottom side is characterized by 0% scalar concentration.

Snapshots of the streamwise velocity obtained at constant z are presented in Fig. 2 from the three different subdomains at different downstream locations as in Fig. 1. A Cartesian system of coordinates is introduced within each of the subdomains of the numerical dataset shown in Fig. 1, where the x axis is oriented along the streamwise direction of the flow, the y axis is oriented along the crosswise (or transverse) direction, and the z axis is oriented along the spanwise direction. These coordinate systems are centered in the upstream and low velocity-side corner in each subdomain. The method for the identification of the internal layers, and for the calculation of the conditional averages of velocities and scalar concentration, is presented in this section.

(1) With the aim of detecting the internal layers, we apply the triple decomposition method introduced by Kolář [30]. A detailed description of the method is presented in Appendix A, and in Nagata *et al.* [31]. According to this method, the velocity gradient tensor can be regarded as constituted by the superposition of three terms corresponding to three elementary flow motions, i.e., a rigid-body rotation, an elongation, and a shear. Schematics representing these elementary flow motions are shown in Fig. 1 of Kolář [30]. In the following equation, the triple decomposition method is formalized, where the terms on the right hand side can be associated with the elementary flow motions of rigid-body rotation, elongation, and shear, and are, respectively, identified with the subscripts RR, EL, and SH:

$$\nabla \mathbf{u} = (\nabla \mathbf{u})_{\text{RR}} + (\nabla \mathbf{u})_{\text{EL}} + (\nabla \mathbf{u})_{\text{SH}}. \quad (1)$$

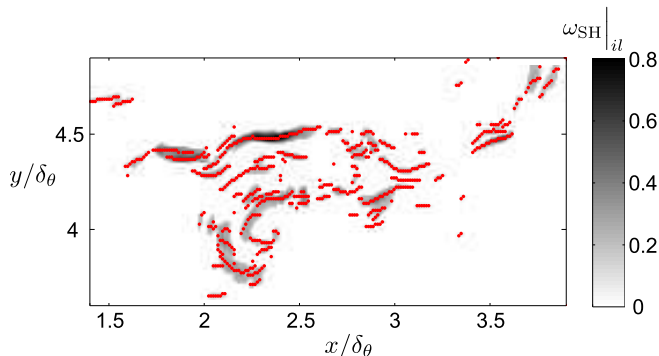


FIG. 3. Snapshot of $\omega_{SH}(x, y, z)|_{il}$ at constant z , within the mixing layer at $Re_\lambda \approx 275$, obtained with $K = 1.5$ in Eq. (2). The streamwise and crosswise coordinates, respectively x and y , are nondimensionalized by the local momentum thickness δ_θ . The red dots are local maxima of $\omega_{SH}(x, y, z)|_{il}$ along the crosswise direction y , and indicate points constituting the internal layers of intense shear.

Among these three terms, only the shear contribution was considered in the calculation of the vorticity magnitude, $|\omega_{SH}(x, y, z)|$. The internal layers are defined as interfaces between adjacent large-scale regions. The difference in momentum between these adjacent large-scale velocity regions produces intense shear at their interface. This motivates the decision of retaining only the shear contribution to the velocity gradient tensor in the calculation of $\omega_{SH}(x, y, z)$. In the continuation of the paper, we identify the magnitude of the shear vorticity as $\omega_{SH}(x, y, z) = |\omega_{SH}(x, y, z)|$. A two-dimensional version of this decomposition was applied by Eisma *et al.* [16] on experimental data of a turbulent boundary layer.

(2) The mean of the shear component of the vorticity magnitude along the z direction is calculated over the entire domain, $\overline{\omega_{SH}}(x, y)$.

(3) At each streamwise location, the maximum of $\overline{\omega_{SH}}(x, y)$ is calculated and the following threshold is applied to identify the internal layers, IL:

$$\omega_{SH}(x, y, z)|_{IL} > K \overline{\omega_{SH}}^{\max, y}(x) \quad (2)$$

where K is a constant. The value of K is chosen to identify only the intense events and, at the same time, to identify a sufficiently large sample to guarantee statistical convergence. In Fig. 2, the regions of intense shear obtained as in Eq. (2), with $K = 1.5$, and marked red are shown on top of the three snapshots of velocity. The condition expressed in Eq. (2) was checked in every point of the domain. In those points where the condition expressed in Eq. (2) is not verified, $\omega_{SH}(x, y, z)|_{IL}$ is set to be equal to zero. A snapshot of $\omega_{SH}(x, y, z)|_{IL}$ is given in Fig. 3, where the intensity of the physical parameter is expressed in shades of gray.

(4) Inside the zones where the condition given in Eq. (2) is verified, the local maxima along the crosswise direction, y , are calculated, at each downstream location. These maxima are considered points of the internal layers (red dots in Fig. 3).

(5) The TNTI, the interface separating a turbulent region from the irrotational external fluid, is detected using a threshold on the vorticity magnitude, which is determined following the method proposed by Taveira and da Silva [32], and summarized in Appendix 1 of Attili *et al.* [8].

(6) Profiles of streamwise velocities centered in the points of internal layers (obtained as explained in step 4) and aligned along the crosswise direction y are identified and retained. These streamwise velocities contribute to the conditional averages that are computed as explained in step 7. Retaining the velocity profiles along the crosswise direction is supported by the assumption that the regions of intense shear vorticity are oriented orthogonal to the mean shear of the flow. This assumption is verified *a posteriori*. Approximately 60% of the regions of intense shear are characterized by an inclination angle with respect to the mean shear Θ in the range $60^\circ < \Theta < 120^\circ$.

An additional reason in support of considering velocity profiles along the crosswise direction is to enable comparisons with the results by Eisma *et al.* [16] and de Silva *et al.* [17]. They analyzed the shear layers in a turbulent boundary layer and reported conditionally averaged profiles along a direction orthogonal to the wall. Only samples located inside the TNTI are retained, and contribute to statistics.

(7) After having identified and retained the profiles of streamwise velocities, these profiles are used to compute the conditional averages. The profiles contributing to the conditional averages are chosen based on the value of u_i , the streamwise velocity in the points constituting the internal layers of intense shear. In the example of Fig. 3, the streamwise velocity u_i determined in the red dots is considered. Intervals of the nondimensional parameter $(\Delta U - u_i)/u_{\text{rms}}$ are identified, where ΔU is the difference in streamwise velocity between the high velocity side and the low velocity side of the mixing layer. These velocity intervals can be related to ranges of crosswise positions within the mixing layer, where larger values of u_i lead to smaller values of the nondimensional parameter $(\Delta U - u_i)/u_{\text{rms}}$. Depending on the value of the streamwise velocity in a point of the internal layers, u_i , the associated velocity profiles contribute to the conditional averages of a given range of $(\Delta U - u_i)/u_{\text{rms}}$. This procedure of conditional averaging is analogous to de Silva *et al.* [17] (see their Figs. 6 and 11).

B. Jet

Internal layers of intense shear are investigated in a turbulent jet with two orifice geometries, a circular orifice and a fractal orifice. The geometry of the fractal orifice is shown in Fig. 1(b) of Breda and Buxton [33]. The two orifices are characterized by identical open areas D_e^2 , where D_e is the equivalent orifice diameter, obtained from the square root of the exit area [Eq. (4) of Breda and Buxton [34]]. The dataset subject of the present analysis was obtained from tomographic particle image velocimetry within a volumetric domain, primarily capturing a radial-azimuthal plane, centered on a downstream location of 25 orifice equivalent diameters, therefore at the end of the developing region. The measurement domain is located in the proximity of the TNTI, and therefore in a region of intense shear that includes both the turbulent and nonturbulent regions, whereas the centerline is not part of the domain. The range of radial positions under analysis is approximately $0 < r/r_{1/2} < 1$, where $r_{1/2}$ is the jet's half width. At the jet orifice, the Reynolds number of both jets is $\text{Re}_{D_e} = 10^4$, where the velocity used in the estimate of the Reynolds number is the equivalent velocity at the orifice, U_e , determined as the ratio between volumetric flow rate over exit area. At 25 equivalent diameters downstream from the jet orifice, at the centerline, the Reynolds number based on the Taylor microscale is $\text{Re}_\lambda \approx 134$ for the circular orifice, and $\text{Re}_\lambda \approx 143$ for the fractal orifice. The interrogation volume was of $48 \times 48 \times 48$ voxels, with a 75% window overlapping. The thickness of the light sheet was of 5 mm. The spatial resolution of the measurement is of 5η , which, with a 75% window overlapping, leads to a vector spacing of 1.25η . The spatial resolution of the tomographic PIV measurement is thus larger than the spatial resolution of 3η prescribed by Worth *et al.* [35] and Buxton *et al.* [36] to resolve the dissipation scales. One of the criteria that is commonly used to assess the adequacy of the spatial resolution to the study of small-scale features is the shape of the joint probability density function (JPDF) of the second and third invariants of the velocity gradient tensor, respectively Q and R . Even if not presented here, the bespoke JPDF has the characteristic tear-drop shape when it is calculated from the present dataset, with a well-developed Viellefosse tail [see Fig. 5.9(c) of Breda [37]]. In addition to this, the dissipation rate calculated from the present dataset of tomographic PIV at a spatial resolution of 5η is compared with the same quantity calculated from planar PIV at a spatial resolution of 3.7η assuming local isotropy, for the same jet flow and at the same downstream distance of 25 orifice equivalent diameters from the orifice. The result of this assessment is presented in Fig. 4 of Breda and Buxton [38], where only a small discrepancy can be observed in the dissipation rate obtained from the two datasets. This suggests that varying the spatial resolution from 3.7η to 5η does not affect the estimated rate of dissipation importantly. This observation is consistent with Tokgöz *et al.* [39], who found that in

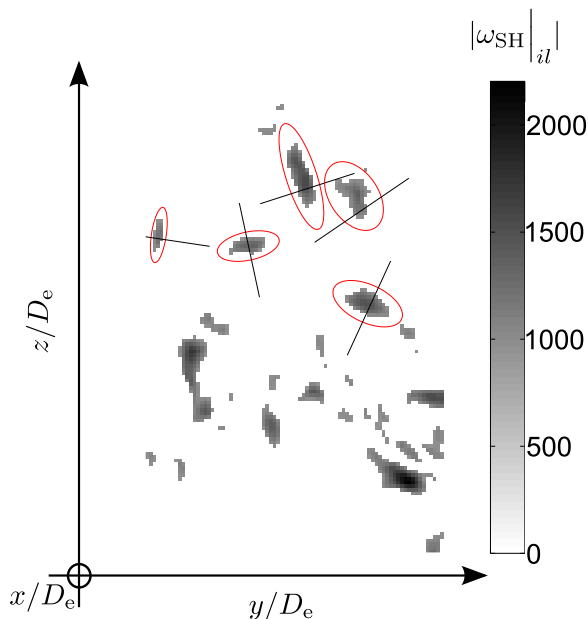


FIG. 4. Snapshot of $\omega_{\text{SH}}(x, y, z)|_{\text{IL}}$ at constant x , within the jet, obtained as explained in Eq. (4). The Cartesian coordinates y and z are nondimensionalized by the equivalent orifice diameter D_e . The red circles are examples of ellipses that were fitted to the zones at intense $\omega_{\text{SH}}(x, y, z)|_{\text{IL}}$, while the black segments orthogonal to the long axes of the fitted ellipses are examples of profiles of the streamwise velocity that are retained in the statistics, thus contributing to the conditionally averaged velocity profiles. Note that profiles of streamwise velocity were determined in each of the points constituting the zones at intense $\omega_{\text{SH}}(x, y, z)|_{\text{IL}}$, and not only where the black segments are drawn. Here, only one segment per zone is presented for clarity.

tomographic PIV a window size of up to eight Kolmogorov length scales with a 75% overlapping is adequate to fully resolve the turbulent dissipation scales. Therefore, the spatial resolution of the present dataset of tomographic PIV is deemed adequate to the goal of the present paper. Further details about the measurement can be found in Breda and Buxton [33], Breda and Buxton [34], and Chap. 2 of Breda [37].

A Cartesian system of coordinates is introduced within this experimental dataset, where the x axis is oriented along the streamwise direction of the flow. The coordinate system is centered in the upstream bottom corner of the measurement domain, therefore in the nonturbulent region (see Fig. 4). The domain has a size of $0.28 \times 1.63 \times 1.85 D_e$, where D_e is the equivalent diameter of the orifice. The location of the domain with respect to the jet is such that increasing values along the y axis correspond to positions closer to the centerline. Although the same symbols are used as the Cartesian system introduced in the dataset of the mixing layer, these symbols can identify the Cartesian system associated with the jet or with the mixing layer depending on whether they refer to one flow or the others.

After decomposing the velocity gradient tensor as shown in Eq. (1), the shear component of the vorticity $\omega_{\text{SH}}(x, y, z)$ was calculated from this dataset. We refer to the *shear component of the vorticity* as SV in the continuation of the paper. With the aim of investigating the internal layers, the TNTI had to be identified. The criterion for the identification of the TNTI is based on enstrophy, as follows:

$$|\omega(x, y, z)|^2 > 0.1 \frac{U_e^2}{D_e^2} \quad (3)$$

where D_e is the equivalent diameter of the orifice and U_e is the equivalent velocity. According to this criterion, the turbulent region is identified when the enstrophy is larger than 10% of the characteristic large-scale vorticity U_e/D_e . The choice of setting an arbitrary threshold for the identification of the TNTI based on the large-scale vorticity of the flow is analogous to previous works examining these interfaces, i.e., Bisset *et al.* [2], Mathew and Basu [40], and da Silva and Pereira [41]. An analysis on the sensitivity of the results to the choice of the threshold value 0.1 in Eq. (3) was conducted. Over the whole range of coefficients examined, it turned out that all the points belonging to the internal layers, identified with the criterion in Eq. (4), remained such for the jet with a fractal orifice. With regard to the round orifice, all the points identified as internal layers remained such for the coefficients 0.025, 0.05, 0.1, and 0.2. For a value of the coefficient of 0.3, 0.73% of the points originally constituting the internal layers ended up becoming external points, whereas for the coefficient being equal to 0.4, this percentage was of 8.95%. It is worth highlighting that the TNTI of the jet flow is not the object of this analysis, but it is determined here only with the aim of discriminating if points of intense shear belong to the turbulent region and should therefore be classified as internal layers, or if they are external to the TNTI. Inside the TNTI, layers of intense SV are identified if more than 12 points of the domain comply with this criterion:

$$\omega_{SH}(x, y, z)|_{IL} > C\omega_{SH}^{rms} \quad (4)$$

where ω_{SH}^{rms} is the rms of the SV magnitude ω_{SH} , and C is a constant.

The condition of Eq. (4) is examined in planes yz , therefore at constant streamwise locations. The internal layers are expected to be oriented orthogonally to the mean shear of the flow. Therefore, while in a mixing layer the internal layers tend to be at a preferential orientation angle with respect to the Cartesian system, the internal layers of a jet can be oriented at any angles in the yz plane. As a consequence, the orientation angles of the internal layers should be determined in a jet if we want to calculate the conditionally averaged profiles of the streamwise velocity across these layers of intense shear. This can be done by fitting an ellipse in each of the zones that are identified with the criterion of Eq. (4), as shown in Fig. 4 for some of the detected zones. A linear least-squares fitting method was employed, which optimizes the squared sum of orthogonal distances from the points to the fitted ellipse. The initial guess is calculated by a linear least-squares routine, using the ‘‘Bookstein constraint’’ (see Gander *et al.* [42]). Local maxima of the SV within the intense zones are calculated along segments orthogonal to the major axis of each fitted ellipse. Profiles of the streamwise velocity centered in these local maxima and oriented orthogonal to the major axis of the associated ellipse (therefore along the minor axis) are estimated. The major axis of the fitted ellipse is used as an approximation for the direction along which a given layer of intense shear develops. The direction orthogonal to the major axis of an ellipse does not necessarily pass through the points of the grid of the PIV velocity dataset, therefore a linear interpolation of the neighboring streamwise velocities is performed to determine the velocity profile along this orthogonal direction. Higher-order methods of interpolation, such as a cubic interpolation and a spline interpolation, are observed to give identical conditionally averaged velocity profiles to the linear interpolation. It is worth stressing that only samples located inside the turbulent region delimited by the TNTI layers contribute to these velocity profiles. Figure 4 shows examples of segments along which the profiles of streamwise velocity are estimated. From these profiles the conditional averages are calculated.

III. INTERNAL LAYERS OF INTENSE SHEAR WITHIN THE MIXING LAYER

The internal layers within the mixing layer are investigated in this section. The conditionally averaged profiles of the streamwise velocity across the internal layers of intense shear are presented in Fig. 5(a). They are obtained as discussed in Sec. II, after setting $K = 1.5$ in Eq. (2). However, it is worth stressing that variations of the constant K do not affect significantly the results of this analysis (see Appendix B for additional details). Three different downstream locations within the flow were examined, corresponding to Reynolds numbers based on the Taylor microscale of $Re_\lambda \approx 200, 250$, and 275. Throughout this paper, the Taylor microscale we use for the nondimensionalization of

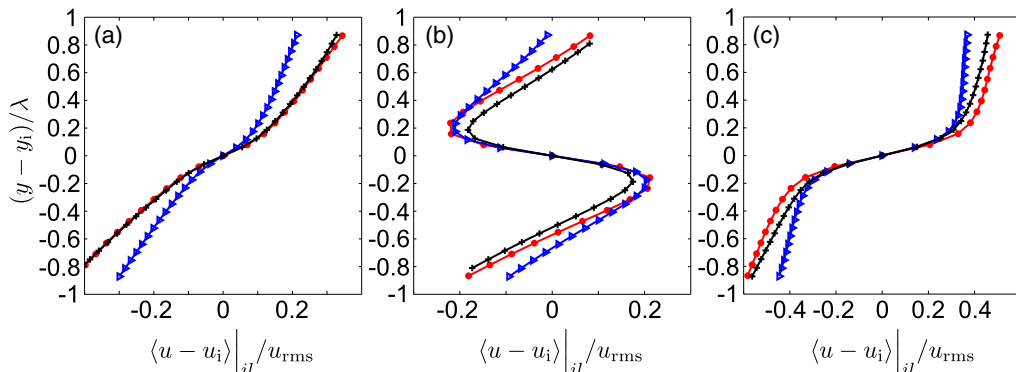


FIG. 5. (a) Conditionally averaged profiles of the streamwise velocity in the near vicinity of *all* detected internal layers within the range $0.25 < (\Delta U - u_i)/u_{\text{rms}} < 0.50$. In (b) and (c), only the profiles characterized by *negative* and *positive* values of $\frac{du}{dy}|_{\text{IL}}$, respectively, were retained and contribute to the conditionally averaged profiles of streamwise velocity. Red full \bullet symbols refer to $\text{Re}_\lambda \approx 200$, black $+$ symbols refer to $\text{Re}_\lambda \approx 250$, and blue empty \triangleright symbols refer to $\text{Re}_\lambda \approx 275$.

the thickness of the internal layers and for the velocity profiles across them is the longitudinal Taylor microscale as defined by Eq. (6.56) of Pope [43], whereas the Taylor microscale we use in the estimate of the Reynolds number Re_λ is the transverse Taylor microscale as defined by Eq. (6.57) of Pope [43]. The choice of using the Taylor length scale to nondimensionalize the velocity profiles in Fig. 5 is consistent with the results from de Silva *et al.* [17] (see their Fig. 12), and from Eisma *et al.* [16] [see their Fig. 8(b)]. All detected internal layers used to compute the velocity profiles in Fig. 5 are characterized by $0.25 < (\Delta U - u_i)/u_{\text{rms}} < 0.50$, where ΔU is the difference in streamwise velocity between the high velocity side and the low velocity side of the mixing layer, and u_{rms} is the velocity *root mean square* calculated at the geometric centerline of the mixing layer. Velocity jumps of modest intensity can be observed to occur across the internal layers of intense shear. Similar velocity jumps were found at different ranges of nondimensional velocities $(\Delta U - u_i)/u_{\text{rms}}$, although not shown here. These velocity jumps can be quantified by applying a fitting to the linear branches of the conditionally averaged profiles, similar to de Silva *et al.* [17] [their Fig. 7(b)]. According to this quantification, the nondimensional velocity jumps $(\delta u)/u_{\text{rms}}$ can be estimated to be of 0.17 and 0.11, respectively, for $\text{Re}_\lambda \approx 200$ and 275. This is one order of magnitude lower than the velocity jumps observed by Ishihara *et al.* [21] in homogeneous isotropic turbulence, which was quantified from instantaneous snapshots of the intense shear layers.

The conditional velocity profiles presented in Fig. 5(a) do not distinguish between negative or positive crosswise gradients of the streamwise velocity $\frac{du}{dy}|_{\text{IL}}$. If we apply this additional conditioning as shown in Fig. 6, i.e., on the sign of $\frac{du}{dy}|_{\text{IL}}$, we obtain the velocity profiles presented in Figs. 5(b) (*negative* crosswise gradients) and 5(c) (*positive* crosswise gradients). Both the velocity profiles exhibit much larger jumps than those in Fig. 5(a). In particular, they are one order of magnitude larger than the velocity jumps of the profiles including all the internal layers, which are given in Fig. 5(a), and of the same order of magnitude as u_{rms} . The internal layers in which the profiles are characterized by $\frac{du}{dy}|_{\text{IL}} > 0$ over the total profiles are found between 60 and 70%, depending on the nondimensional velocity $(\Delta U - u_i)/u_{\text{rms}}$, i.e., on the crosswise position within the flow, and on the local Reynolds number. Therefore, as expected, profiles with $\frac{du}{dy}|_{\text{IL}} > 0$ are dominant, which explains the similar trends observed in Figs. 5(a) and 5(c). A significant percentage of the velocity profiles at the internal layers (between 30 and 40%) is characterized by *negative* $\frac{du}{dy}|_{\text{IL}}$, which leads to mild velocity jumps when all the detected internal layers are considered in the computation of the conditionally averaged profiles [Fig. 5(a)]. The structures that could be associated with these

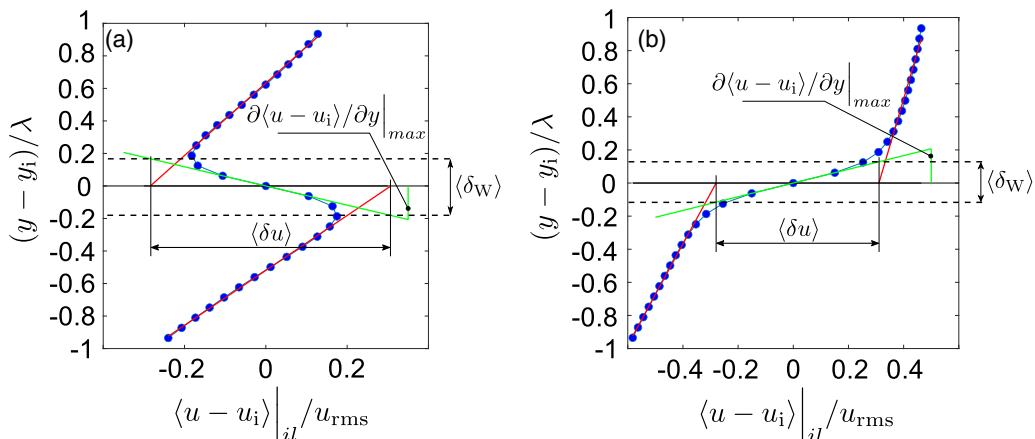


FIG. 6. Averaged conditional statistics for the streamwise velocity across the internal layers of intense shear after distinguishing into (a) *negative* and (b) *positive* crosswise gradients of the streamwise velocity, $\frac{du}{dy}|_{IL}$. The quantities $\langle \delta u \rangle$, $\partial \langle u - u_i \rangle / \partial y|_{max}$, and $\langle \delta_w \rangle$ correspond to the jump in the averaged streamwise velocity, the maximum local gradient of the averaged profile, and the characteristic thickness of the internal layer, respectively. In this figure, the profiles at $Re_\lambda \approx 250$ from Fig. 5 are used.

conditionally averaged profiles are internal layers of intense shear of the same type as those that are associated with the profiles characterized by *positive* values of $\frac{du}{dy}|_{IL}$, with the only difference that the local high velocity side of these internal layers is on the opposite side with respect to the high velocity side of the mixing layer flow, and the same applies for the low velocity side. Internal layers are small-scale features, therefore features tending to isotropy to the limit of an infinite Reynolds number. Nonetheless, averaging all of them, and therefore considering the net contribution of all these internal layers, results in the mean flow, i.e., the macroscopic mixing layer, which is anisotropic. This means that although the internal layers characterized by a *positive* $\frac{du}{dy}|_{IL}$, thus oriented as the mean flow, are dominant in a probabilistic sense, there is a large number of them that are oriented in the completely opposite way. Different ranges of $(\Delta U - u_i)/u_{rms}$ produce velocity profiles analogous to those presented in Fig. 5, even if they are not shown here for brevity.

In Figs. 7 and 8, the streamwise and crosswise components of the local advection velocities of the points constituting the internal layers of intense shear are presented. The streamwise local velocities within the internal layers are evaluated at the three different streamwise locations, corresponding to Reynolds numbers based on the Taylor microscale of $Re_\lambda \approx 200, 250,$ and 275 . The internal layers are identified using two values of K in Eq. (2), i.e., $K = 1.5$ and 2.5 . The black continuous lines and the blue dashed lines represent the average streamwise velocities of the points constituting the internal layers, calculated, respectively, for $K = 1.5$ and 2.5 , at a range of crosswise positions. The gray regions bound a range of velocities characterized by $\bar{u}_i \pm \sigma(u_i)$, where $\sigma(u_i)$ is the standard deviation of the velocities at the points constituting the internal layers, i , and u_i are the streamwise velocities at the points i . The red dots represent the average streamwise velocities of the flow. The position of the geometric centerline is shown with vertical continuous lines, while the crossing points in the average streamwise velocity are shown with vertical dashed lines. The internal layers of intense shear tend to be more preferentially located where the mean shear is maximum, therefore in the vicinity of the crossing point of the average streamwise velocity (red dots) in Fig. 7, while this probability tends to gradually decrease where both TNTIs are approached. A mild scattering of the blue and black lines can be observed as the edge of each plot is approached, thus when moving towards both TNTIs, which can be attributed to a not sufficiently large statistical sample to reach a complete statistical convergence. The described scattering occurs more prominently when

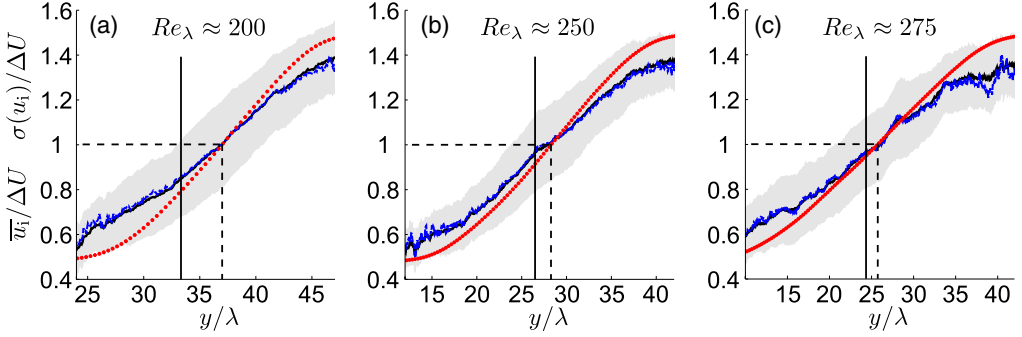


FIG. 7. Black continuous lines show the average values of the instantaneous streamwise velocities \bar{u}_i of all the points representing the internal layers as detected from Eq. (2), with $K = 1.5$, at different nondimensional crosswise locations y/λ . The gray region bounds the instantaneous streamwise velocities within the range $\bar{u}_i \pm \sigma(u_i)/\Delta U$, where σ is the standard deviation. Blue dashed lines represent the same as black continuous lines, but the coefficient in Eq. (2) is $K = 2.5$. Red full \bullet symbols are the average streamwise velocity of the flow. Vertical continuous lines identify the geometric centerlines, while dashed lines identify the crossing points within the flow, therefore the physical centerlines. These features are investigated at (a) $Re_\lambda \approx 200$, (b) $Re_\lambda \approx 250$, and (c) $Re_\lambda \approx 275$.

retaining only the more intense events (blue lines), which are fewer in number. Moreover, increasing streamwise positions, associated with larger Reynolds numbers, determines a crosswise spread of the mixing layer, which results in smaller statistical samples and larger levels of scattering too, as can be observed when looking at Fig. 7(c). The main aspect that can be observed in Fig. 7 is that near the high velocity side of the flow the internal layers are characterized by a local advection velocity lower than the average velocity of the flow, while near the low velocity side of the flow the opposite occurs. This observation is consistent with Buxton *et al.* [44], Buxton and Ganapathisubramani [45], and Fiscaletti *et al.* [28] (their Figs. 2 and 3). The reversal of the observed behavior, i.e., the crossing point where the average velocity of the internal layers overlaps with the average velocity of the flow, is not at the geometric centerline, but at a crosswise position closer to the

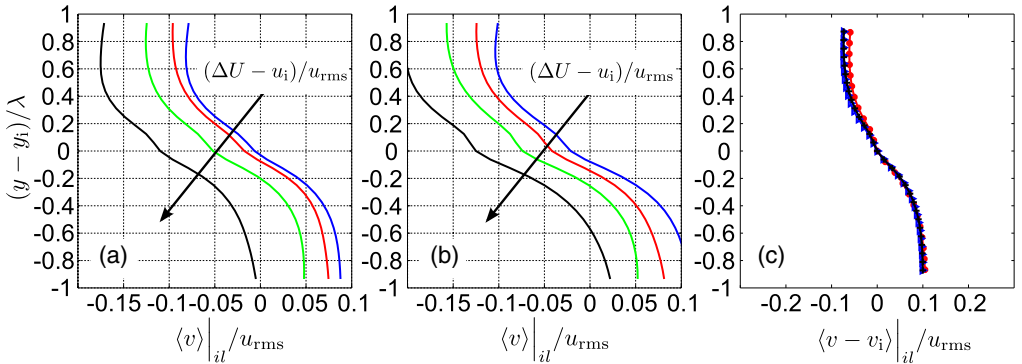


FIG. 8. (a), (b) Conditionally averaged profiles of crosswise velocity in the near vicinity of (a) all the points representing the internal layers, and (b) only those points characterized by positive values of $\frac{du}{dy}|_{IL}$ detected within the ranges (blue line) $-0.25 < (\Delta U - u_i)/u_{rms} < 0$, (red line) $0 < (\Delta U - u_i)/u_{rms} < 0.25$, (green line) $0.25 < (\Delta U - u_i)/u_{rms} < 0.50$, and (black line) $0.50 < (\Delta U - u_i)/u_{rms} < 0.75$. (c) Conditionally averaged profiles of crosswise velocity with respect to the local crosswise velocity at the internal layers, within the range $0.25 < (\Delta U - u_i)/u_{rms} < 0.50$, at $Re_\lambda \approx 200, 250$, and 275 (symbols defined as in Fig. 5).

low velocity side of the flow with respect to the geometric centerline of the mixing layer itself. In Fig. 7, it can be observed that for increasing Reynolds number, therefore when moving along the streamwise direction, the nondimensional distance between the geometric centerline and the crossing point tends to diminish. However, it is important to stress that this absolute distance tends to increase overall, and the observation from Fig. 7 is the result of the Taylor microscale increasing more rapidly. Therefore, the increasing downstream location accentuates the mismatching between the crossing point and the geometric centerline and, as a consequence, the crossing point presents growing displacements towards the low velocity region of the flow when moving downstream. The velocity difference between the average velocity and the local streamwise velocity of the internal layers tends to increase when moving towards both the TNTIs. The described trends appear to be insensitive to the value of the constant K .

The averages of the crosswise advection velocities of points constituting the internal layers are presented in Fig. 8, at different velocity ranges $(\Delta U - u_i)/u_{\text{rms}}$. In Fig. 8(a), all the internal layers are considered, while in Fig. 8(b) only the profiles of the internal layers characterized by *positive* values of the crosswise gradients of streamwise velocities $\frac{du}{dy}|_{\text{IL}}$ are considered. From this analysis, we can see that the internal layers of intense shear tend to move on average from the high velocity side to the low velocity side of the mixing layer. This crosswise velocity tends to increase for increasing values of the quantity $(\Delta U - u_i)/u_{\text{rms}}$, thus when approaching the low velocity side of the flow. Larger crosswise velocities can also be observed when examining only the internal layers with *positive* values of the crosswise gradients [Fig. 8(b)]. In Fig. 8(c), the crosswise velocity profiles relative to the velocity at the internal layers, v_i , are shown, at the three different Reynolds numbers $\text{Re}_\lambda \approx 200, 250, \text{ and } 275$. From this analysis, positive crosswise velocities (upwash) are found on the lower side of the internal layers, while negative crosswise velocities (downwash) are found on the upper side of the internal layers. These velocities profiles appear to be insensitive to the Reynolds number.

The velocity jumps of the internal layers at the three different Reynolds number and at the different ranges of nondimensional velocities $(\Delta U - u_i)/u_{\text{rms}}$ are presented in Fig. 9. Specifically, Figs. 9(a) and 9(c) report the strength of the velocity jumps associated with profiles where $\frac{du}{dy}|_{\text{IL}} > 0$, while in Figs. 9(b) and 9(d) the velocity jumps are associated with profiles where $\frac{du}{dy}|_{\text{IL}} < 0$. In the top figures, the velocity jumps are nondimensionalized by the r.m.s. velocity, while in the bottom figures the nondimensionalization is done by the large-scale quantity ΔU , the velocity difference across the mixing layer. As can be observed in Fig. 9, velocity jumps of more than 10% of ΔU are found in a statistical sense across the identified layers of intense shear. Also, $\langle \delta u \rangle$ appears not to depend on the range of nondimensional velocities where these intense shear layers are detected. This is different from what was found in a turbulent boundary layer, where larger velocity jumps were detected closer to the wall, therefore at increasingly larger momentum deficits (Eisma *et al.* [16], de Silva *et al.* [17]). It can also be observed that these velocity jumps nondimensionalized by the constant quantity ΔU are characterized by decreasing intensities for growing Re_λ , both for positive and negative gradients of $\frac{du}{dy}|_{\text{IL}}$ [Figs. 9(c) and 9(d)]. In turbulent boundary layers, the increasingly larger velocity jumps detected when moving closer to the wall could be explained as an effect of the local Reynolds number of the flow. As the wall approaches, the local Reynolds number of the flow decreases, which results in larger velocity jumps, consistent with the relationship between Reynolds number and velocity jump across the internal layers that is found in this paper and in previous ones, e.g., Elsinga *et al.* [20].

The velocity jumps across intense shear layers that are quantified in the present mixing layer can be compared with those found in different turbulent flows. From DNS of homogeneous isotropic turbulence at very large Re_λ , Ishihara *et al.* [21] examined instantaneous snapshots of extreme shear events. The authors reported velocity jumps of the order of the velocity r.m.s., which is consistent with the finding of the present analysis (Fig. 9). From their analysis on DNS data of both a channel flow and a turbulent boundary layer, Wei *et al.* [46] reported velocity jumps of approximately half the r.m.s. velocity [their Fig. 6(d)]. Similar to Wei *et al.* [46], de Silva *et al.* [17] and Eisma *et al.* [16]

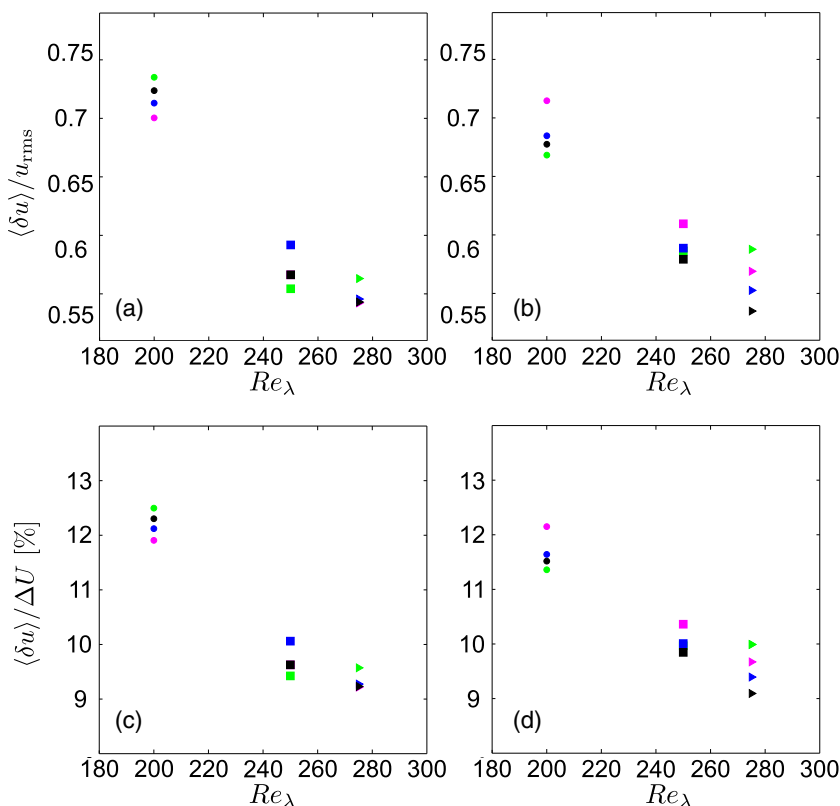


FIG. 9. Velocity jump at the internal layers identified by setting $K = 1.5$ in Eq. (3) for (a), (c) positive and (b), (d) negative values of $\frac{du}{dy}|_{\text{IL}}$ detected within the ranges (green symbols) $-0.25 < (\Delta U - u_i)/u_{\text{rms}} < 0$, (magenta) $0 < (\Delta U - u_i)/u_{\text{rms}} < 0.25$, (blue) $0.25 < (\Delta U - u_i)/u_{\text{rms}} < 0.50$, and (black) $0.50 < (\Delta U - u_i)/u_{\text{rms}} < 0.75$. \bullet symbols refer to $Re_\lambda \approx 200$, \blacksquare symbols refer to $Re_\lambda \approx 250$, and \blacktriangleright symbols refer to $Re_\lambda \approx 275$.

reported smaller velocity jumps than those obtained here from their experimental investigations on turbulent boundary layers [see Fig. 13(b) of de Silva *et al.* [17] and Fig. 8(a) of Eisma *et al.* [16]]. The smaller values of the velocity jumps compared to those in the aforementioned studies on turbulent boundary layers can be attributed to the conditioning of averages on the sign of the transverse gradients. When not conditioning on the sign of these gradients, much smaller velocity jumps are obtained in the present paper too, which can also be qualitatively appreciated from comparing Figs. 5(a) with 5(b).

Following Brown and Roshko [47], the thickness of the internal layers of intense shear δ_w can be estimated as the ratio between the velocity jump δu and the maximum local gradient of the profile $\partial \langle u - u_i \rangle / \partial y|_{\text{max}}$. The thicknesses of the internal layers associated with profiles with $\frac{du}{dy}|_{\text{IL}} > 0$ and with $\frac{du}{dy}|_{\text{IL}} < 0$, obtained as illustrated in Fig. 6, are presented, respectively, in Figs. 10(a) and 10(c) and in Figs. 10(b) and 10(d). These thicknesses are nondimensionalized by the Taylor microscale λ [Figs. 10(a) and 10(b)] and by the Kolmogorov microscale η [Figs. 10(c) and 10(d)], and estimated at different Re_λ , i.e., different streamwise locations, and at different ranges of streamwise velocities $(\Delta U - u_i)/u_{\text{rms}}$.

From Fig. 10, it is not possible to establish whether the thickness of the internal layers scales with the Taylor length scale or with the Kolmogorov length scale. This is because the range of Reynolds

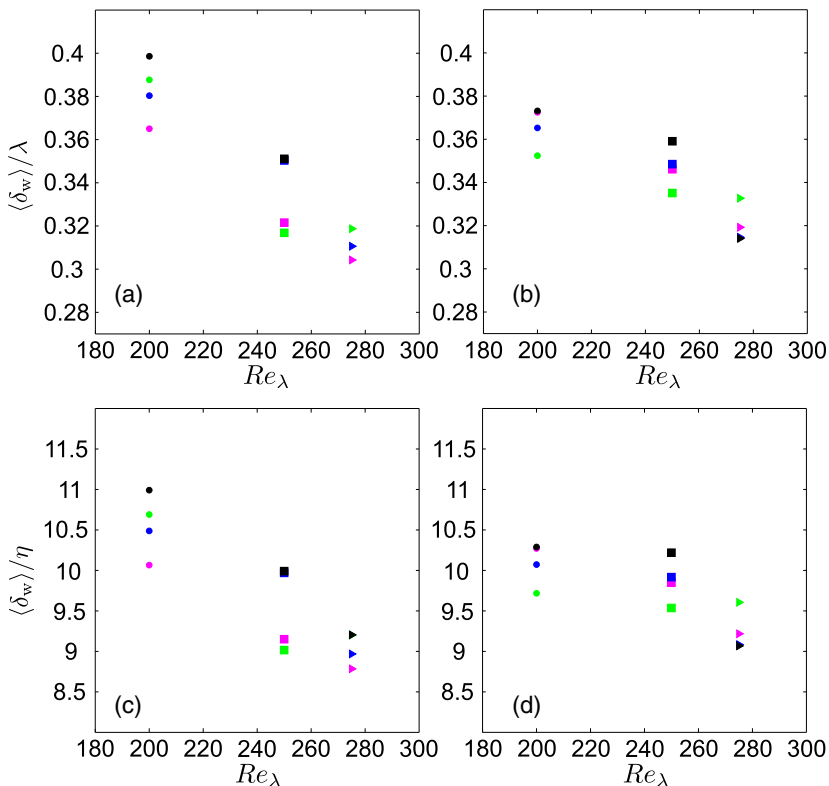


FIG. 10. Thickness of the internal layers identified by setting $K = 1.5$ in Eq. (3) for (a), (c) *positive* and (b), (d) *negative* values of $\frac{du}{dy}|_{IL}$ detected within the ranges (green symbols) $-0.25 < (\Delta U - u_i)/u_{rms} < 0$, (magenta) $0 < (\Delta U - u_i)/u_{rms} < 0.25$, (blue) $0.25 < (\Delta U - u_i)/u_{rms} < 0.50$, and (black) $0.50 < (\Delta U - u_i)/u_{rms} < 0.75$. \bullet symbols refer to $Re_\lambda \approx 200$, \blacksquare symbols refer to $Re_\lambda \approx 250$, and \blacktriangleright symbols refer to $Re_\lambda \approx 275$.

number under analysis is not sufficiently large. However, several important observations can be made. First, the thickness of the internal layers seems to be insensitive to the velocity range $(\Delta U - u_i)/u_{rms}$. Secondly, $\langle \delta_w \rangle / \lambda$ ranges between 0.3 and 0.4, which is the same as that found by Eisma *et al.* [16] [their Fig. 8(b)], and very similar to what found by de Silva *et al.* [17] [their Fig. 13(e)] in turbulent boundary layers. Moreover, $\langle \delta_w \rangle / \eta$ is nearly equal to 10, which is the characteristic diameter of the small-scale coherent structures according to several studies, the so-called worms [21,48–51]. It can also be observed that $\langle \delta_w \rangle$ decreases when moving from $Re_\lambda \approx 200$ to 275. This is analogous to what was observed for the velocity jump, $\langle \delta u \rangle$.

IV. INTERNAL LAYERS OF INTENSE SHEAR WITHIN THE JET

The internal layers of intense shear are investigated in the jet with two different orifice geometries, a circular and a fractal orifice. The near field of the circular jet is characterized by intense coherent structures developing in the azimuthal direction, whereas the fractal orifice was observed to break the azimuthal coherence, which changes significantly the near field of turbulence [33,34]. In the past, several studies showed that changes of the initial conditions of a jet have a strong impact on the fully developed region of a jet (see Xu and Antonia [52] and references therein). In this section, we intend to examine if and how different orifice geometries could affect the characteristics

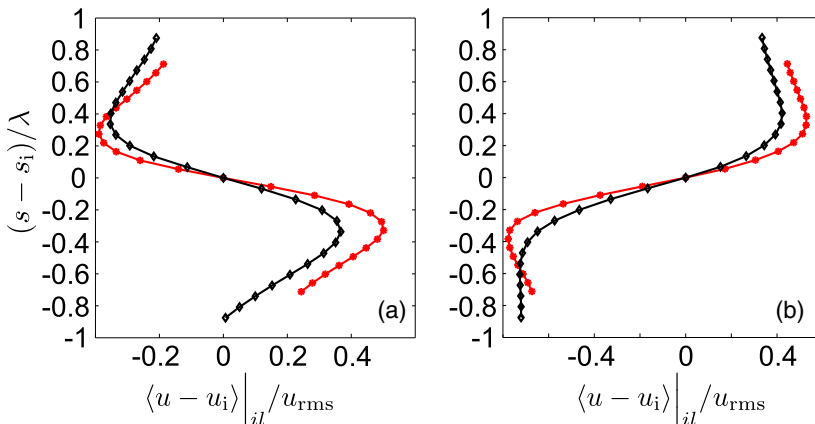


FIG. 11. Conditionally averaged profiles of the streamwise velocity in the near vicinity of the internal layers of intense shear, in which only the profiles characterized by (a) *negative* and (b) *positive* values of $\left. \frac{du}{ds} \right|_{\text{IL}}$ are retained and contribute to the calculation. Red \bullet symbols refer to the circular jet, while black \blacklozenge symbols refer to the fractal jet.

of the internal layers, at the beginning of the fully developed region of the flow, i.e., at a downstream distance of 25 diameters. Moreover, a different free-shear flow at a different Reynolds number is analyzed to determine a scaling for the thickness of the internal layers.

In the jet, the internal layers are obtained as discussed in Sec. II, after setting $C = 3$ in Eq. (4). However, variations of the constant C do not affect significantly the results of this analysis, as shown in Appendix C. The profiles of streamwise velocity are presented in Fig. 11 along a local abscissa s that passes through the point s_i of the region of intense shear, and has a direction orthogonal to the major axis of the fitted ellipse. We distinguish between negative and positive gradients of the streamwise velocity $\left. \frac{du}{ds} \right|_{\text{IL}}$, analogous to the analysis of the mixing layer in Sec. III. The sign of the gradient of the streamwise velocity $\left. \frac{du}{ds} \right|_{\text{IL}}$ for each profile is determined based on the sign of the gradient of the conditional mean streamwise velocity along the segments where the velocity profiles are calculated, i.e., along the local abscissa s . Positive gradients are those where the sign of the local gradient agrees with the gradient of the mean streamwise velocity, and vice versa. Red circles refer to the circular jet, while black diamonds represent the fractal jet. As can be seen, the shapes of the two profiles are similar to conditionally averaged profiles obtained from the mixing layer (in Fig. 5), and they do not appear to be particularly sensitive to the initial conditions of the flow. Similar to the mixing layer, the percentage of velocity profiles characterized by negative transverse gradients, therefore having an opposite sign with respect to the mean shear, is of 31% for the jet with a fractal orifice, and it is of 34% for the jet with a round orifice. Therefore, the sign of the transverse gradients across the internal layers is in prevalence coherent to the mean shear of the region of jet flow under analysis. There is however a significant percentage of internal layers in which the shear is opposite with respect to the mean shear, similar to the mixing layer.

From the analysis of the conditionally averaged profiles, we can determine the velocity jump across the layers. Both with a circular and a fractal orifice, velocity jumps larger than the velocity r.m.s. are obtained. Specifically, $\langle \delta u \rangle / u_{\text{rms}}$ is equal to 1.24 for the fractal jet and to 1.57 for the jet with circular jet, when positive transverse gradients are considered. $\langle \delta u \rangle / u_{\text{rms}}$ is equal to 1.14 for the fractal jet and to 1.33 for the circular jet, when negative transverse gradients are considered. The velocity r.m.s. used for the nondimensionalization, u_{rms} , is calculated using samples of the flow domain in the point where the average streamwise velocity is maximum. The obtained u_{rms} is expected to be analogous to the rms at the jet centerline as it is calculated in a point in the range $0 < r/r_{1/2} < 1$, a range of radial locations over which u_{rms} does not vary significantly according to the

literature on jets (see Pope [43]). These velocity jumps are larger than the velocity jumps obtained in the mixing layer [Figs. 9(a) and 9(b)]. This can be either the consequence of a different flow or of a lower Reynolds number. The second explanation seems to be more convincing considering the trend reported in Figs. 9(a) and 9(b), where at decreasing Reynolds numbers we observe larger velocity jumps, for the same flow. Increasing velocity jumps nondimensionalized by u_{rms} for decreasing Reynolds numbers are consistent with the observations by Gul *et al.* [19] on a pipe flow, by Wei *et al.* [46] on wall-bounded flows [their Fig. 6(d)], and by Elsinga *et al.* [20] on homogeneous isotropic turbulence (their Figs. 4 and 19). In the latter two works, the maximum tangential velocity in the direction orthogonal to the shear layer was examined, which can be assimilated to half of the velocity jump as defined in the present paper. When nondimensionalized by the jet velocity at the orifice, the velocity jumps found in the jet are of the order of 10%, which is comparable to what we find in the mixing layer [Figs. 9(c) and 9(d)]. These findings confirm what we observe from the analysis of the mixing layer, i.e., that in free-shear flows velocity jumps across the internal layers are considerably larger than in previous analyses on wall-bounded flows. Similar to the comment made when examining the mixing layer, this discrepancy can be attributed to not having accounted for the sign of the wall-normal gradients of the streamwise velocity when computing the conditional averages.

From the velocity profiles in Fig. 11, we can determine the characteristic thickness of the internal layers. When nondimensionalized by the Taylor microscale, we obtain that $\langle \delta_w \rangle / \lambda$ is equal to 0.51 for the fractal jet and to 0.47 for the circular jet, when positive transverse gradients are considered. $\langle \delta_w \rangle / \lambda$ is equal to 0.66 for the jet with fractal orifice and to 0.50 for the jet with circular orifice, when negative transverse gradients are examined. For the jet, a nondimensionalization of the characteristic thickness $\langle \delta_w \rangle$ by the Kolmogorov length scale would be challenging though, as the Kolmogorov length scale is heavily dependent on the position within the flow and affected by measurement noise. Moreover, the velocity data from the jets do not include the geometric centerline, therefore it would be inaccurate to use estimates of the Kolmogorov length scale at the centerline. It was therefore decided not to quantify the thickness of the internal layers within the jets in terms of Kolmogorov length scale, but only in terms of Taylor microscale. From this analysis, it appears that the thickness of the internal layers at a downstream distance from the jet orifice of 25 diameters is not significantly affected by changes in the jet initial conditions.

Overall, when comparing these values with those obtained from the analysis of the mixing layer, it appears that the thickness of the internal layers decreases with the local Reynolds number. The thickness of the internal layers of intense shear identified in the jet and in the mixing layer and nondimensionalized by the Taylor microscale is presented in Fig. 12 for varying Reynolds numbers. The ratio $\langle \delta_w \rangle / \lambda$ closely follows the scaling law $\langle \delta_w \rangle / \lambda \sim \text{Re}_\lambda^{-1/2}$. From recalling that at high Reynolds numbers the ratio between the Kolmogorov and the Taylor microscales is $\eta / \lambda \sim \text{Re}_\lambda^{-1/2}$, the observed scaling law $\langle \delta_w \rangle / \lambda \sim \text{Re}_\lambda^{-1/2}$ suggests a Kolmogorov scaling for the thickness of the internal layers of intense shear in free-shear flows. The observed scaling for the internal layers is consistent with the very recent observations of Watanabe *et al.* [53], who examined the shearing motions in isotropic turbulence with the same triple decomposition as that applied in the present paper. However, Eisma *et al.* [16] and de Silva *et al.* [17] found a Taylor scaling for the internal layers from the analysis of turbulent boundary layers, although in their analysis de Silva *et al.* [17] adopted a different methodology than the one used in the present paper. Therefore, a possible explanation for the observed difference between the present result and the Taylor scaling found by de Silva *et al.* [17] could be attributed to the methodology to identify the internal layers within the flow. Regarding the investigation of Eisma *et al.* [16], they applied an identification criterion similar to the one adopted here, but they did not account for the sign of the crosswise gradient when determining the average profiles across the internal layers, which could lead to a larger thickness. It is worth highlighting that recently Silva *et al.* [12] found a Kolmogorov scaling also for the thickness of the TNTI in the range of Reynolds number $142 \leq \text{Re}_\lambda \leq 400$. This finding expands from previous observations by Holzner and Lüthi [54], Watanabe *et al.* [13], and Watanabe *et al.* [14].

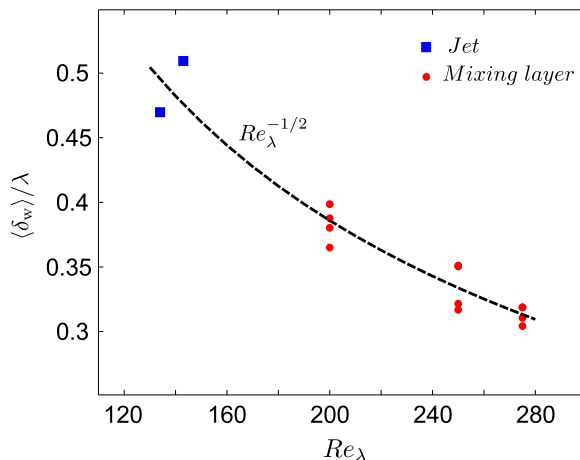


FIG. 12. Thickness of the internal layers identified in the jet (blue ■) and in the mixing layer (red ●) as explained in Sec. II, and normalized by the Taylor microscale λ , as a function of the Reynolds number Re_λ .

V. THE CONCENTRATION OF A PASSIVE SCALAR ACROSS THE INTERNAL LAYERS

In the following, we focus on the concentration of a passive scalar across the internal layers. According to the analysis presented up until now and to the previous literature, several features of the internal layers are common to the TNTI. These are (i) the existence of a jump in the streamwise velocity profile, (ii) the scaling of the jump thickness, and (iii) the entrainment of fluid associated with the observed velocity jumps. Given the existing analogies between the TNTI and the internal layers, and given that also the scalar concentration exhibits a jump across the TNTI, as Gampert *et al.* [5] (their Fig. 15) and Gampert *et al.* [6] (their Fig. 10) showed, we might also expect to find a jump of scalar across the internal layers. If such a jump was observed, it would mean that zones of relatively uniform scalar concentration are bounded by internal layers of intense shear throughout the flow. Conditional averages of a passive scalar at Schmidt number $Sc = 1.4$ are calculated across the internal layers, and they are reported in Fig. 13. As can be observed, the concentration of a passive scalar does not exhibit any jumps $\langle \delta c \rangle$ across the internal layers. In a similar way, there seem

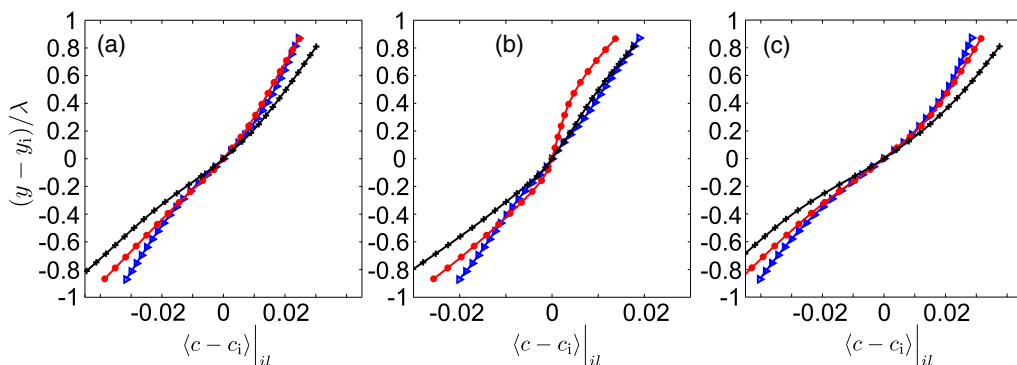


FIG. 13. (a) Conditionally averaged profiles of scalar concentration at Schmidt number $Sc = 1.4$ in the near vicinity of *all* detected internal layers within the range $0.25 < (\Delta U - u_i) / u_{rms} < 0.50$, in the DNS mixing layer. In (b) and (c), only the *negative* and *positive* values of $\frac{du}{dy}|_{IL}$, respectively, are retained and contribute to the conditionally averaged profiles of streamwise velocity. Symbols are defined in Fig. 5.

to be no jumps when applying an additional conditioning on the sign of the crosswise gradient $\frac{du}{dy}|_{IL}$, as shown in Figs. 13(b) and 13(c). This observation can be confirmed from a rigorous quantification of $\langle \delta c \rangle$ analogous to that made for the jumps in the streamwise velocity $\langle \delta u \rangle$, and illustrated in Sec. III. The described quantification results in concentration jumps one order of magnitude smaller than those computed from streamwise velocity profiles (Fig. 9), from which we can consider them as negligible. Although not reported here, a similar analysis is also performed for a passive scalar at Schmidt number $Sc = 0.7$ and 0.35 . The results are analogous to those obtained at Schmidt number $Sc = 1.4$, which shows that small deviations of the Schmidt number from unity do not significantly affect the concentration of a passive scalar in the proximity of the internal layers.

From this analysis, layers of intense shear are not characterized by strong crosswise gradients of a passive scalar. Therefore, the internal layers, which bound regions of different momentum, do not appear to bound regions of different passive scalar according to our finding from Fig. 13. It is worth pointing out that this finding is independent of the method that is adopted for the identification of these internal layers. A method analogous to the one described in de Silva *et al.* [17] can also be applied, with the aim of identifying the internal layers. This method relies on the local probability density function for the identification of the edges of “uniform momentum zones,” which are regarded as the internal layers within turbulent boundary layers. Even if additional details of this analysis are not reported here for the sake of brevity, conditionally averaged profiles analogous to those presented in Fig. 13 are obtained when applying such a methodology. These observations are consistent with Brethouwer *et al.* [25], who performed numerical simulations of isotropic turbulence at relatively low Reynolds numbers and at a wide range of Schmidt numbers. They found that the scalar gradients are weak in regions of intense vorticity.

VI. INTERNAL LAYERS OF INTENSE SCALAR GRADIENT

In this section, the reverse problem is investigated. Starting from the points at intense scalar gradients, we intend to examine the profiles of average streamwise velocity in the proximity of these points. We shorten *scalar gradient* as SG in the continuation of the paper. Three snapshots of the magnitude of the SG $|\nabla c(x, y, z)|$ at Schmidt number $Sc = 1.4$ and at $Re_\lambda \approx 250$ are shown in Fig. 14. From this figure, it can be observed that the passive scalar is organized into thin layers of intense SG which appear to be elongated along the streamwise direction, and therefore their orientation tends to be nearly orthogonal with respect to the mean shear of the flow. The points constituting layers of intense magnitude of the SG are identified with the following method:

$$|\nabla c(x, y, z)|_{GSC} > H |\nabla c(x, y, z)|^{\max, yz}(x) \quad (5)$$

where GSC stands for *gradient of scalar concentration* and denotes the identification of a layer of intense gradient of scalar concentration. According to Eq. (5), a point (x, y, z) is considered part of an internal layer of intense SG if $|\nabla c(x, y, z)|$ is larger than the local maximum along the y and z directions multiplied by a constant. At each Reynolds number, the distribution of points of intense SG along the crosswise direction (not shown here for brevity) exhibits a maximum in the proximity to the geometric centerline of the mixing layer, even though a more uniform spread over the crosswise direction can be observed when compared with the points of intense shear. After setting $H = 0.4$, conditionally averaged profiles of the streamwise velocity are computed across $|\nabla c(x, y, z)|_{GSC}$. These profiles are presented in Fig. 15, at different Reynolds numbers and at different ranges of velocities $(\Delta U - u_i)/u_{rms}$. It is worth stressing that the profiles in Fig. 15 consider all the points identified with Eq. (5), and therefore they do not distinguish among profiles of positive or negative crosswise gradient of the streamwise velocity, $\frac{du}{dy}$, as done in obtaining Figs. 5(b) and 5(c).

From Fig. 15, jumps in the streamwise velocity appear along the crosswise direction. The strength of these jumps seems to mildly decrease at increasing Reynolds number. Also, the positive branches

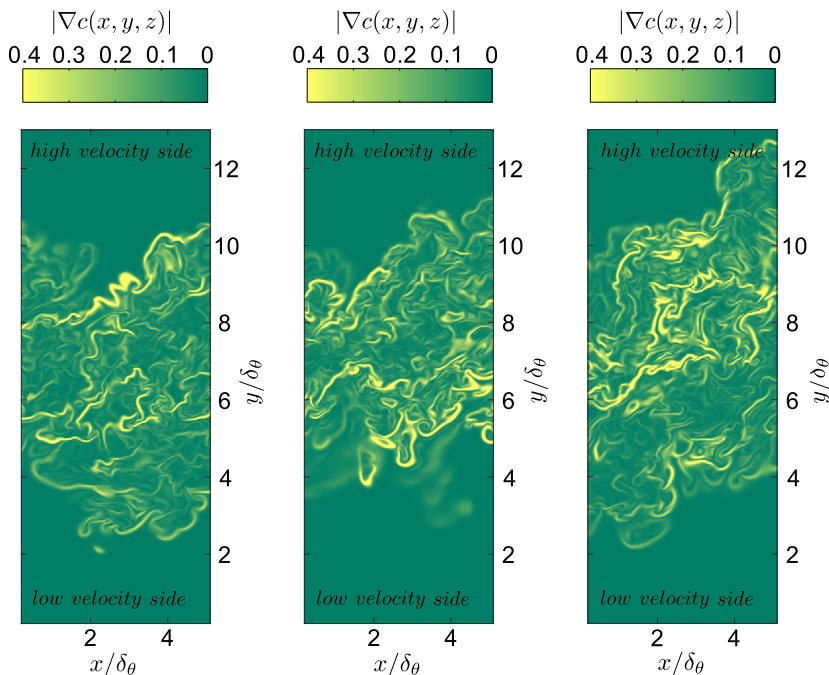


FIG. 14. Snapshots showing the magnitude of $\nabla c(x, y, z)$ on planes at constant z , in a streamwise region where $\text{Re}_\lambda \approx 250$. The streamwise and crosswise coordinates, respectively x and y , are nondimensionalized by an averaged momentum thickness δ_θ in this region.

of the velocity profiles are inclined at increasing angles with respect to the vertical, at increasing values of $(\Delta U - u_i)/u_{\text{rms}}$, thus when moving towards the low velocity side of the mixing layer. On the other hand, a counterclockwise rotation of the negative branches appears for growing $(\Delta U - u_i)/u_{\text{rms}}$. The velocity profiles obtained in the vicinity of the layers of intense SG can be compared with those obtained in the previous section, which are conditioned on the internal layers of intense shear, and are shown in Fig. 5(a). The latter profiles are composed of three straight lines, and the velocity jump occurs over a crosswise span of $0.2\text{--}0.3\lambda$, whereas the profiles conditioned on the intense SG show a milder but constant velocity variation, and the jump occurs over a crosswise span of $0.5\text{--}0.6\lambda$. These differences in the velocity profiles evidence a different flow topology between the layers of intense shear and the layers of intense SG.

The observed difference in the topological content can be further investigated through the analysis of the second and third invariants of the velocity gradient tensor, Q and R [55]. In the following, we examine the statistics of the Q and R invariants. We first consider random points of the flow domain included between the TNTIs, then we consider only the points that are part of the internal layers of intense shear, and, finally, only the points characterized by intense $|\nabla c(x, y, z)|$. In Figs. 17(a), 17(b), and 17(c) the results of this analysis are presented. A conventional division of the JPDF of the Q and R invariants into four regions was proposed by Ooi *et al.* [56], and their lifetime and temporal evolution in turbulent flows was investigated more recently by Elsinga and Marusic [57]. The described classification of the local flow topology based on the Q and R invariants is shown in Fig. 16. According to this classification, region I corresponds to stable focus/stretching [$R > 0$, $Q > -(27R^2/4)^{1/3}$], region II corresponds to unstable focus/stretching [$R < 0$, $Q > -(27R^2/4)^{1/3}$], region III corresponds to stable node/saddle/saddle [$R > 0$, $Q < -(27R^2/4)^{1/3}$], and region IV corresponds to unstable node/saddle/saddle [$R < 0$, $Q < -(27R^2/4)^{1/3}$].

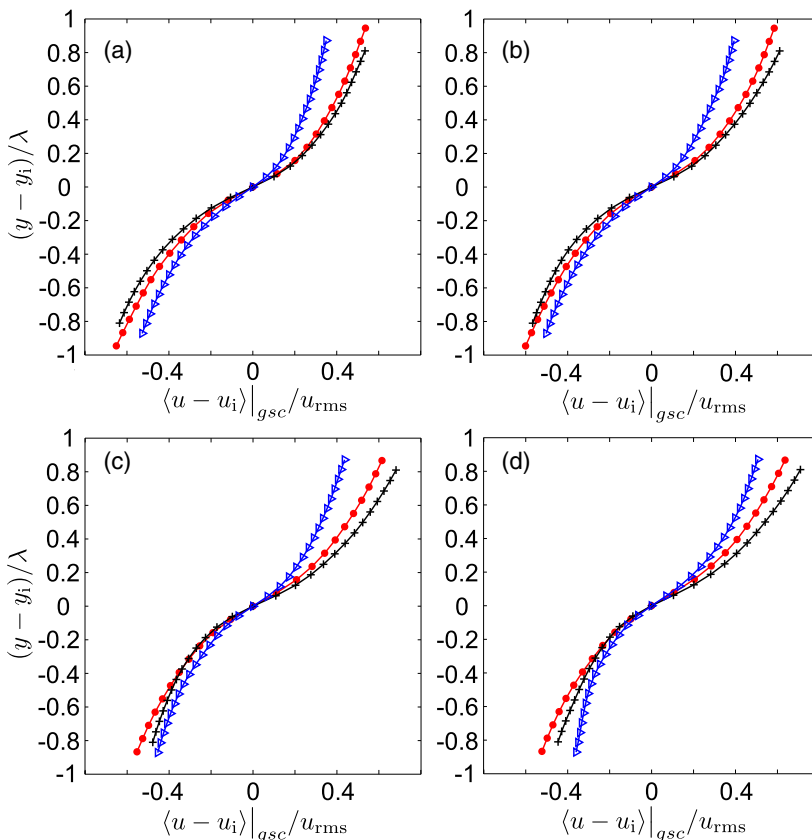


FIG. 15. Conditionally averaged profiles of the streamwise velocity in the near vicinity of crosswise gradients of the passive scalar concentration at Schmidt number $Sc = 1.4$ within the range (a) $-0.25 < (\Delta U - u_i)/u_{rms} < 0$, (b) $0 < (\Delta U - u_i)/u_{rms} < 0.25$, (c) $0.25 < (\Delta U - u_i)/u_{rms} < 0.50$, and (d) $0.50 < (\Delta U - u_i)/u_{rms} < 0.75$. \bullet symbols indicate $Re_\lambda \approx 200$, $+$ symbols indicate $Re_\lambda \approx 250$, and \triangleright symbols indicate $Re_\lambda \approx 275$.

Figure 17(a) shows the JPDF of the second and third invariants calculated in random points of the turbulent domain. Over 5×10^6 points are used in these statistics, identified at constant intervals along the three directions of the flow, within the turbulent region. The isocontours of the JPDF exhibit the characteristic tear-drop shape, with the tail along the right branch of the null-discriminant line into region II, and the body inclined towards region I. This shape was observed in several previous investigations of turbulent flows [56–60], and it is considered a universal characteristic of small-scale turbulence according to Elsinga and Marusic [23]. A similar JPDF is obtained when the Q and R invariants are calculated in points that are part of the internal layers of intense shear [Fig. 17(b)], after setting $K = 2.5$ in Eq. (2), with the aim of considering the most extreme events only. However, this result is not particularly sensitive to the value of the constant K , as discussed in Appendix D. The observed analogy between the unconditional JPDF and the JPDF obtained at the internal layers of intense shear shows that the latter ones are characterized statistically by a very similar topological content as any other random points within the turbulent flow. The JPDF of the second and third invariants of the velocity gradient tensor presents the characteristic tear-drop shape in points of intense shear vorticity, even though slightly skewed towards region I, which is associated with stable focus/stretching (see Fig. 16). The topology of focus/stretching results is dominant over node/saddle/saddle, with a 75% probability. From the analyses presented in

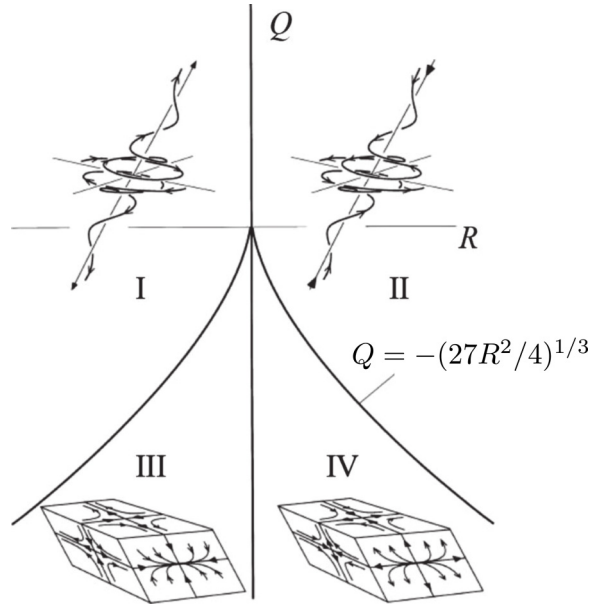


FIG. 16. Local flow topologies associated with the invariants of the velocity gradient tensors (Q and R) for incompressible flow. Region I corresponds to stable focus/stretching [$R > 0$, $Q > -(27R^2/4)^{1/3}$], region II corresponds to unstable focus/stretching [$R < 0$, $Q > -(27R^2/4)^{1/3}$], region III corresponds to stable node/saddle/saddle [$R > 0$, $Q < -(27R^2/4)^{1/3}$], and region IV corresponds to unstable node/saddle/saddle [$R < 0$, $Q < -(27R^2/4)^{1/3}$]. Figure adapted from Ooi *et al.* [56].

Secs. III and IV, the internal layers of intense shear scale with the Kolmogorov microscale, which implies that these internal layers are small-scale dissipative features. Their thickness is also found to be of approximately $9-11\eta$. The JPDF in Fig. 17 shows that the points constituting the internal layers of intense shear are characterized by a dominant flow topology of stable focus/stretching (region I of Fig. 16). Such a flow topology is associated with the elongated coherent structures of vorticity that can be typically identified in small-scale turbulence, the so-called worms, with a characteristic diameter of approximately 10η [21,48–51]. All these aspects concur with the development of a conceptual picture for these internal layers as constituted by a series of line vortices, the worms, organized into vortex sheets, and bounding regions of large and intermediate length scales, consistent with the model proposed by Hunt *et al.* [22]. Therefore, the identified internal layers are cuts through the structures of vortex sheets (see Fig. 3), with their major axis being preferentially oriented orthogonally to the observation plane.

A different topological content is found when considering only points characterized by intense magnitude of the SG. These are points of the three-dimensional domain where the concentration of a passive scalar exhibits a large gradient, and they are identified after setting $H = 0.6$ in Eq. (5). The JPDF of the Q and R invariants in points of intense SG is presented in Fig. 17(c). As can be observed, the Q and R invariants are preferentially located in regions I and IV, although the JPDF of the Q and R invariants also extends to region III. On the other hand, the statistical presence of the Q and R invariants inside region II is nearly insignificant, which is an important difference with respect to Fig. 17(a). The tail located along the right branch of the null-discriminant line is also much longer here than in the unconditional JPDF. Therefore, two flow topologies are mainly present in these layers of intense $|\nabla c(x, y, z)|$, which are the unstable node/saddle/saddle and the stable focus/stretching. The strong prevalence of the unstable node/saddle/saddle is evidence that at intense $|\nabla c(x, y, z)|$ strain dominates rotation (Fig. 16). The topology of node/saddle/saddle is prevalent over the focus/stretching topology, with 59% of the total probability. A flow topology

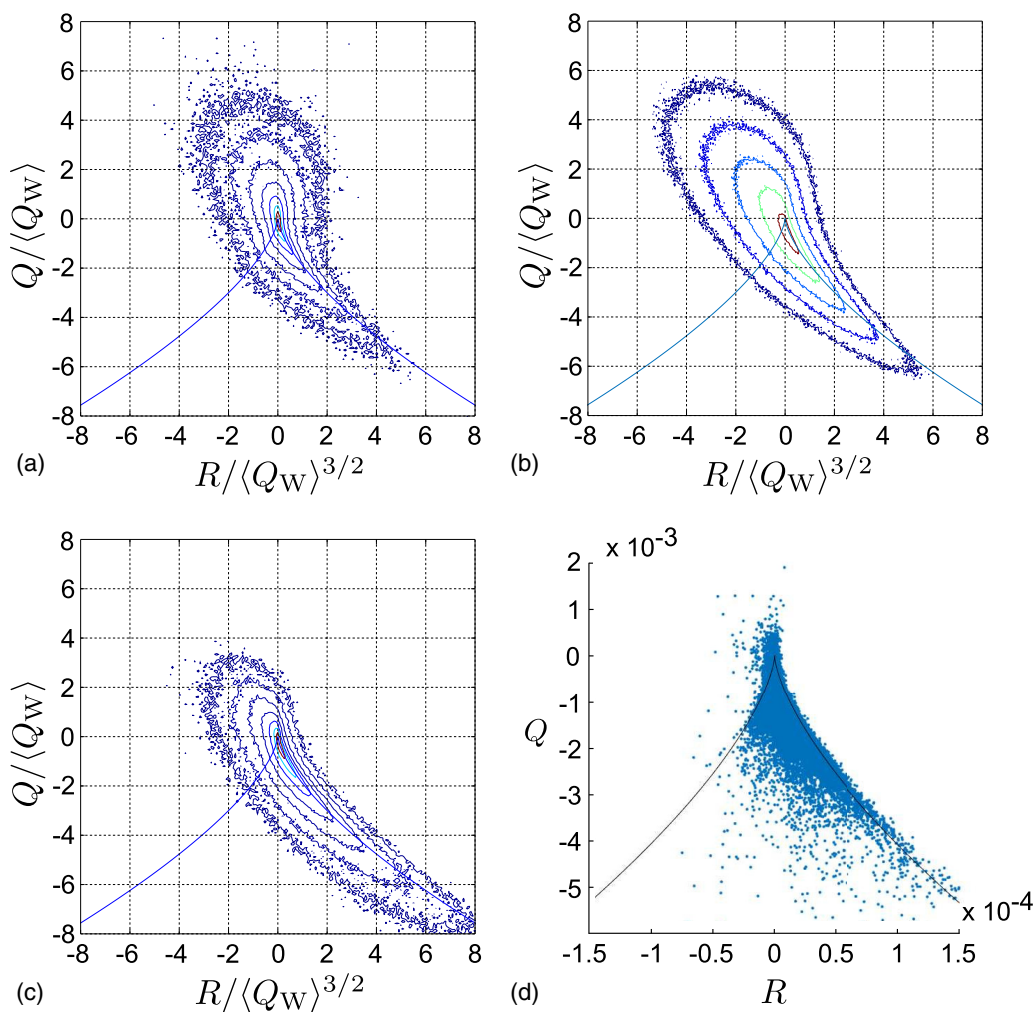


FIG. 17. Joint probability density functions of the second (Q) and third (R) invariants of the velocity gradient tensor (a) in random points of the turbulent portion of the domain, (b) in points of intense shear vorticity $\omega_{\text{SH}}(x, y, z)$, and (c) in points of intense gradient of the scalar concentration $|\nabla c(x, y, z)|$ [with $H = 0.6$ in Eq. (5)], at $\text{Re}_\lambda \approx 275$. (d) QR scatter plot at $y_1 = 4\eta$ from the TNTI of the low velocity side of the flow inside the turbulent region, at $\text{Re}_\lambda \approx 250$. The blue continuous lines are the null-discriminant lines $Q = -(27R^2/4)^{1/3}$ (Chong *et al.* [55]). In each panel, four regions can be identified, and their physical meaning is illustrated in Fig. 16. $Q_w = (\nabla \times \mathbf{u})^2/4$.

of unstable node/saddle/saddle can be associated with diverging streamlines (region I of Fig. 16), and therefore with low levels of mixing in the neighborhood of the point, which explains the high gradient of scalar concentration. On the other hand, in a flow topology of stable focus/stretching the streamlines are associated with the formation of a vortex. This enhances mixing of the scalars, which reduces the local norm of the scalar concentration gradient, thus leading to the conditionally averaged profiles of scalar concentration presented in Fig. 13. Variation of the coefficient H in Eq. (5) does not affect significantly the results reported in Fig. 17(c), as discussed in Appendix D. These observations on the topological content of points at intense SG are consistent with Brethouwer *et al.* [25] and Elsinga and da Silva [24], among others.

In Fig. 17(d), we present the QR scatter plot of points located at $y_1 = 4\eta$ from the TNTI of the low velocity side of the flow inside the turbulent region, at $Re_\lambda \approx 250$. Note that $y_1 = 4\eta$ represents the envelope of the TNTI at a crosswise distance of 4η . This location is approximately at the interface between the viscous superlayer (VSL) and the turbulent sublayer (TSL) (see Fig. 1 of da Silva *et al.* [61]), given that the extent of the VSL is of $4-5\eta$ according to Taveira and da Silva [62] and Silva *et al.* [12]. The Q and R invariants are preferentially located in regions I, III, and IV, with a prevalence for the topology of node/saddle/saddle. This result is consistent with Taveira and da Silva [62], who showed that the production of enstrophy $\omega_i S_{ij} \omega_j$ becomes significant at $\simeq 5\eta$, which suggests that a prevalence of foci is expected to build up at this location. Although not reported here, scatter plots are also estimated in points at $y_1 = 2\eta$ and 6η . From these plots we can infer that for decreasing distances from the TNTI, the Q and R invariants tend to be more preferentially located in region III and less preferentially located in region I, consistent with Elsinga and da Silva [24] (their Fig. 7). The observation reported in Fig. 17(d) is an important analogy with the prevalent flow topology that characterizes the layers of intense $|\nabla c(x, y, z)|$. In this mixing layer, and, predictably, in other turbulent flows, several similarities exist between the internal layers of intense SG and the TNTI. These are (i) the existence of a velocity jump across both types of layers, (ii) the existence of a jump in the concentration of a passive scalar across both types of layers (this is by definition true in layers of intense SG), (iii) a topological content characterized by a prevalence of node/saddle/saddle and stable focus/stretching, and (iv) an overall dominance of unstable node/saddle/saddle, which is evidence that strain is dominant. Moreover, the findings from the analysis given in Fig. 17 explain why the conditionally averaged profiles of scalar concentration shown in Fig. 13 have a uniform trend, i.e., they do not exhibit any discontinuities or jumps. The lack of jumps in the scalar profiles suggests that the gradients of the scalar concentration tend to not be located within the internal layers of intense shear. Therefore, regions of intense scalar gradients and layers of intense shear vorticity are not expected to spatially overlap. The analysis of the flow topology in points of intense scalar gradients and in points of intense shear vorticity confirms this inference by showing that they are characterized by a different topological content. Because the flow topology of unstable node/saddle/saddle is dominant at intense scalar gradients while the stable focus/stretching is dominant in the internal layers of intense shear, scalar gradient and shear vorticity tend to be located in different regions of the flow.

From the profiles of streamwise velocity conditioned on the intense SG (Fig. 15), we observe that a jump in the streamwise velocity occurs in layers of intense SG. Analogous velocity jumps are identified in the internal layers of intense shear. Although we stress that a difference exists in the prevalent topological content between points of intense shear and points of intense SG, it is not clear what is their mutual location within the turbulent flow. We try therefore to answer the question “given that the chances are small for scalar and velocity gradient to overlap, is there a preferential location where we could find a point of intense scalar gradient with respect to a point of intense shear vorticity?” This aspect can be investigated from the covariance between SV and SG. This analysis was performed for the mixing layer at $Re_\lambda \approx 275$, in the range of crosswise positions $y = [5.1, 6.5]$, and it is presented in Fig. 18. The results are obtained from averaging the covariance along the spanwise direction, which is calculated in 348 uncorrelated planes along the streamwise and crosswise directions. The covariance has the physical dimension of $[m^{-1} s^{-1}]$. The largest covariance is found for a nearly zero displacement, which means that the SV correlates with the SG, although weakly. Comparable values are found for positive streamwise displacements Δx up to $\approx 4\lambda$, and for negative crosswise displacements Δy up to $\approx -2.5\lambda$. From the analysis of the topological content of the points at intense SG, we can see that it is highly improbable that the QR invariants are located in region II of the QR JPDF [where $R > 0$ and $Q > -(27R^2/4)^{1/3}$, see Fig. 16]. From this observation, points of intense SV belonging to the region II are not expected to correlate with points of intense SG, simply because there are very small chances that they share the same flow topology. According to this reasoning, these points are set to zero in the SV dataset, and the covariance between this and the SG are calculated in the same way as explained previously. The results of this calculation are presented in Fig. 19. At nearly zero displacements, a covariance

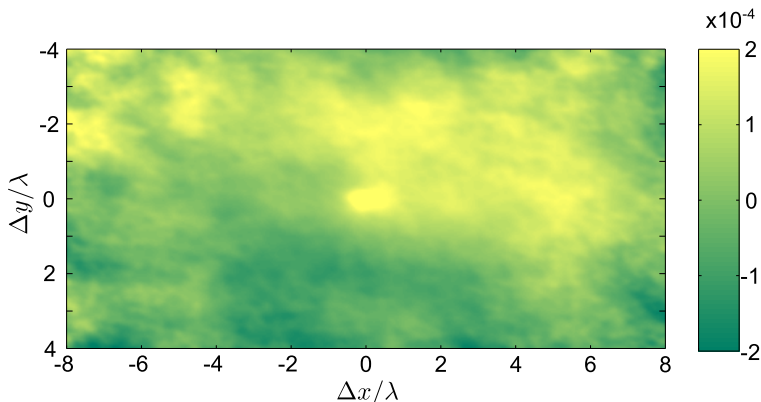


FIG. 18. Covariance between the shear vorticity magnitude ω_{SH} and the scalar gradient magnitude $|\nabla c|$ in the range of crosswise positions $y = [5.1, 6.5]$, at $\text{Re}_\lambda \approx 275$.

double that obtained previously is found in this case. Furthermore, these levels of covariance are much larger than those obtained far from $\Delta y \approx \Delta x \approx 0$, which shows that SV correlates locally with SG when points belonging to region II are not considered. These points account for only 25% of the total turbulent region, at $\text{Re}_\lambda \approx 275$.

After having ascertained that the SV correlates locally with the SG, we examine the probability of points of intense SV to overlap with points of intense SG. Therefore, the following analysis tries to answer the question “what is the probability that a point of intense SV is also a point of intense SG, and vice versa?” The results are presented in Table I. As can be observed, an overlap probability larger than 10% (up to 15% for $\text{Re}_\lambda \approx 250$) is obtained when examining whether points of intense SG are also points of intense SV ($|\nabla c| \mapsto \omega_{\text{SH}}$), with the latter ones being identified after setting $K = 1.5$ in Eq. (2). On the other hand, a probability slightly larger than 2% is estimated when examining whether points of intense SV are also points of intense SG ($\omega_{\text{SH}} \mapsto |\nabla c|$). This shows that there is a much larger probability that a point of intense SG is also a point of intense SV, rather than the other way around, although this is still unlikely to occur. This finding is consistent with the conditionally averaged profiles reported in Figs. 13 and 15, i.e., it is consistent with finding a velocity jump across the internal layers of intense SG, and with not finding any jumps in the

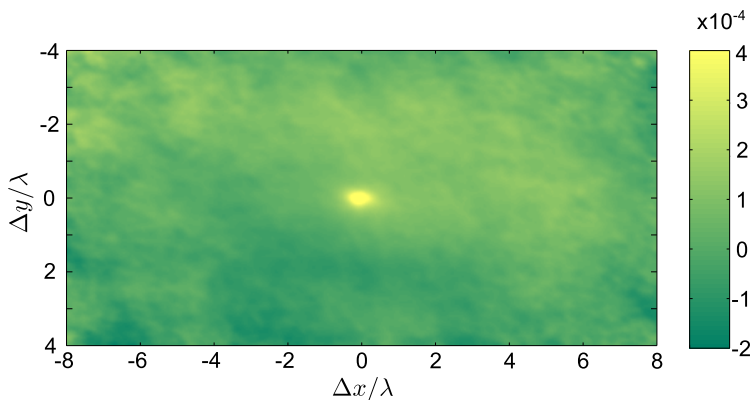


FIG. 19. Covariance between the shear vorticity magnitude ω_{SH} and the scalar gradient magnitude $|\nabla c|$ after removing points characterized by unstable focus/stretching, in the range of crosswise positions $y = [5.1, 6.5]$, at $\text{Re}_\lambda \approx 275$.

TABLE I. Probability that a point of intense shear vorticity, ω_{SH} , is also a point of intense SG, $|\nabla c|$, and vice versa. The points of intense shear vorticity are identified for $K = 1.5$ and 2.5 [Eq. (2)], while the points of intense SG are identified for $H = 0.4$ [Eq. (5)], and at three different Reynolds numbers.

K	H		Re_λ		
			200	250	275
1.5	0.4	$\omega_{\text{SH}} \mapsto \nabla c $	2.5%	2.4%	1.9%
		$ \nabla c \mapsto \omega_{\text{SH}}$	10.7%	15.9%	12.0%
2.5	0.4	$\omega_{\text{SH}} \mapsto \nabla c $	2.5%	3.1%	2.3%
		$ \nabla c \mapsto \omega_{\text{SH}}$	2.2%	3.9%	2.5%

scalar concentration across layers of intense shear. This observation is also consistent with recent experimental analyses presented by van de Water *et al.* [63], who examined the dispersion of a plume of pollutant in a turbulent boundary layer. Nonetheless, when the identification of the intense internal layers is made by setting $K = 2.5$ in Eq. (2), a drop in the percentage probability is obtained. This suggests that points at intense SG tend to be located where the SV is larger than average, even though they are not preferentially located in the extreme shear events within the flow.

VII. CONCLUSIONS

In this paper, internal layers were investigated both in a mixing layer and in a jet, in the range of Reynolds numbers based on the Taylor microscale $134 < \text{Re}_\lambda < 275$. The mixing layer was obtained from DNS while the jet under analysis came from experiments of tomographic PIV where two different orifice geometries were adopted, a fractal orifice and a circular orifice.

Internal layers of intense shear were identified after applying a triple decomposition of the velocity gradient tensor into the sum of three different contributions, i.e., rigid-body rotation, elongation, and shear, in which only the shear component was used in the calculation of the vorticity. In the turbulent domain, the magnitude of the shear vorticity was required to be larger than a threshold value in order to identify an internal layer of intense shear. The identified internal layers of intense shear tend to move on average from the high velocity side to the low velocity side of the mixing layer, therefore with a negative crosswise velocity. This crosswise velocity tends to increase for increasing values of the quantity $(\Delta U - u_i)/u_{\text{rms}}$, thus when approaching the low velocity side of the flow. The local advection velocity of the points constituting the internal layers of intense shear was also assessed. Near the high velocity side of the flow the internal layers are characterized by a local advection velocity lower than the average velocity of the flow, while near the low velocity side of the flow the opposite occurs. This is consistent with recent observations from the literature.

Across all detected internal layers, conditionally averaged profiles of streamwise velocity exhibited jumps that, if made nondimensional by the velocity r.m.s., showed a decreasing trend for increasing Re_λ . The observed velocity jumps accounted for approximately 10% of the characteristic large-scale velocity of the flow, which is in a mixing layer the velocity difference between the high and the low velocity sides, and in a jet, the orifice velocity. The intensity of these velocity jumps is much larger than what Eisma *et al.* [16] and de Silva *et al.* [17] found in turbulent boundary layers. From the conditionally averaged profiles of streamwise velocity, we estimated the characteristic thickness of the internal layers of intense shear. We found that, in the mixing layer, this thickness does not depend significantly on the crosswise location, and it is between 0.3 and 0.4 times the Taylor microscale, and of between 9 and 11 times the Kolmogorov microscale. The thickness of these internal layers is analogous to what is reported in turbulent boundary layers when nondimensionalized by the Taylor microscale.

From the analysis of the mixing layer solely, it was not possible to determine whether the thickness of the internal layers scales with the Taylor or with the Kolmogorov microscale, because the range of Re_λ under investigation was not sufficiently large. The results from the jet at $\text{Re}_\lambda \approx 140$

were therefore added to the analysis on the mixing layer with the aim of determining a scaling for the thickness of the internal layers. In the jet, a thickness of around $\langle \delta_w \rangle \approx 0.5\lambda$ was estimated, independent of the orifice geometry. When considering both flows for scaling purpose, we found that $\langle \delta_w \rangle / \lambda \sim \text{Re}_\lambda^{-1/2}$, which suggested that $\langle \delta_w \rangle$ scales with the Kolmogorov length scale (Fig. 12). Recently, Silva *et al.* [12] observed that also the TNTI scales with the Kolmogorov microscale, which appears to be an important analogy between the internal layers of intense shear and the TNTI. However, these two types of layers exhibit a major difference in the way the concentration of a passive scalar (at $\text{Sc} = 1.4$) varies across them. While previous literature showed that a jump exists in the scalar concentration across the TNTI, no jumps were found across the internal layers of intense shear.

With the aim of explaining this difference of behavior, the topological content of the flow was examined in points characterized by an intense magnitude of the scalar gradient. It was found that node/saddle/saddle and stable focus/stretching are prevalent (Fig. 16), with an overall dominance of node/saddle/saddle, which is associated with strain. A very similar topological content was observed in the proximity of the TNTI, whereas the internal layers are shear-dominated regions. The JPFD of the second and third invariants of the velocity gradient tensor presents the characteristic tear-drop shape in points of intense shear vorticity, even though slightly skewed towards region I, which is associated with stable focus/stretching. The observed different content in the flow topology between shear vorticity and scalar gradient explained the absence of a jump in the profiles of scalar concentration across the shear layers. On the other hand, when conditionally averaged profiles of streamwise velocity were calculated across layers of intense scalar gradient, evidence of velocity jumps was found. These observations showed that the TNTI presents more similarities with the layers of intense scalar gradient than with the layers of intense shear. In particular, the similarities between the TNTI and the layers of intense scalar gradient are (i) the existence of a velocity jump, (ii) the existence of a scalar jump across both types of layers, (iii) the topological content, and (iv) an overall dominance of strain over rotation.

The cross correlation between shear vorticity and scalar gradient was calculated to determine possible mutual interactions between these quantities. A weak peak was found for a nearly zero displacement along the streamwise and crosswise directions. However, when the points characterized by unstable focus/stretching were removed from the map of shear vorticity, a stronger correlation peak was obtained, of double intensity. This showed that unstable focus/stretching within the shear vorticity can dramatically deteriorate the levels of correlation between shear vorticity and scalar gradient. Finally, the probability that a point of intense scalar gradient is also a point of intense shear vorticity, and vice versa, was examined. A point of intense scalar gradient has more than 10% chance of being also a point of intense shear vorticity, whereas the opposite is much more improbable, accounting for a probability of 2–3%.

In future works, it would be of interest to examine whether significant deviations of the Schmidt number from unity, therefore when either viscous diffusion or molecular diffusion is dominant, could affect the characteristics and the topological content of the internal layers of intense scalar gradient. The effect of Schmidt numbers in the range $0.07 \leq \text{Sc} \leq 7.0$ on the structure of the scalar gradient near the TNTI of a planar jet was investigated in the recent past by Silva and da Silva [64]. Higher Schmidt numbers produce a steeper scalar gradient jump in the TNTI and a more corrugated interface of the passive scalar at the jet edge. Also, the outer boundary of the TNTI based on the scalar gradient tends to coincide with the TNTI obtained from vorticity at $\text{Sc} = 7.0$, whereas at decreasing Schmidt numbers their distance becomes progressively larger.

APPENDIX A: THE TRIPLE DECOMPOSITION OF THE VELOCITY GRADIENT TENSOR

The triple decomposition of the velocity gradient tensor is illustrated in this Appendix. The decomposition is performed in the frame of reference that maximizes the quantity $G = |S_{12}\Omega_{12}| + |S_{23}\Omega_{23}| + |S_{31}\Omega_{31}|$, where \mathbf{S} and $\mathbf{\Omega}$ are, respectively, the strain-rate tensor and the vorticity tensor. We define this new frame of reference the *basic reference frame* (BRF), following the nomenclature

by Kolář [30]. The velocity gradient tensor $\nabla \mathbf{u}^*$ in the BRF frame is obtained as $\mathbf{Q}(\nabla \mathbf{u})\mathbf{Q}^T$, where \mathbf{Q} is the transformation tensor for an arbitrarily rotated Cartesian coordinate system, and it can be obtained by a sequence of three rotational transformations with respect to the Cartesian system introduced in Sec. II. The first rotation of an angle α , with $0 \leq \alpha \leq \pi$, is around the z axis. The second rotation of an angle β , with $0 \leq \beta \leq \pi$, is around the y axis obtained from the previous transformation. The third rotation of an angle γ , with $0 \leq \beta \leq \pi/2$, is around the z axis obtained from the previous two transformations. In the following, the transformation tensor $\mathbf{Q}(\alpha, \beta, \gamma)$ is presented:

$$\mathbf{Q} = \begin{bmatrix} \cos\alpha \cos\beta \cos\gamma - \sin\alpha \sin\gamma & \sin\alpha \cos\beta \cos\gamma + \cos\alpha \sin\gamma & -\sin\beta \cos\gamma \\ -\cos\alpha \cos\beta \sin\gamma - \sin\alpha \cos\gamma & -\sin\alpha \cos\beta \sin\gamma + \cos\alpha \cos\gamma & \sin\beta \sin\gamma \\ \cos\alpha \sin\beta & \sin\alpha \sin\beta & \cos\beta \end{bmatrix}.$$

In implementing this transformation, the values of the three angles α , β , and γ are varied, each of them at increments of multiples of $\Delta = \pi/12$. The sensitivity of the results to the size of the increment angle Δ was tested. It was found that for $\Delta < \pi/9$ the results are not significantly affected. This observation is consistent with Nagata *et al.* [31].

Each combination of the so obtained triplets of angles identifies a distinct frame of reference. In each of these frames of reference, the quantity G is calculated. The frame of reference in which the quantity G is the highest identifies the BRF frame of reference. The velocity gradient tensor $\nabla \mathbf{u}$ is calculated in BRF. In this new frame of reference BRF, the velocity gradient tensor is referred to as $\nabla \mathbf{u}^*$. Two contributors to $\nabla \mathbf{u}^*$ can be identified, i.e., $(\nabla \mathbf{u}^*)_{\text{RES}} = (\nabla \mathbf{u}^*)_{\text{EL}} + (\nabla \mathbf{u}^*)_{\text{RR}}$ and $(\nabla \mathbf{u}^*)_{\text{SH}}$, where $\nabla \mathbf{u}^*_{\text{SH}}$ identifies the *shear* contribution, while $\nabla \mathbf{u}^*_{\text{RR}}$ and $\nabla \mathbf{u}^*_{\text{EL}}$ represent the contributions from the *rigid body rotation* and *elongation*, respectively. The shear contribution of the velocity gradient tensor $\nabla \mathbf{u}^*$ can be obtained from the following relationship [see Eq. (8b) of Kolář [30]]:

$$[(\nabla \mathbf{u}^*)_{\text{RES}}]_{ij} = \text{sgn}[(\nabla \mathbf{u}^*)_{ij}] \min[|(\nabla \mathbf{u}^*)_{ij}|, |(\nabla \mathbf{u}^*)_{ji}|]$$

where $\text{sgn}(h)$ is the sign function that yields $\text{sgn}(h) = 1$ for $h > 0$, $\text{sgn}(h) = 0$ for $h = 0$, and $\text{sgn}(h) = -1$ for $h < 0$. The component $(\nabla \mathbf{u}^*)_{\text{SH}}$ can be obtained from subtracting $(\nabla \mathbf{u}^*)_{\text{RES}}$ to $\nabla \mathbf{u}^*$. In order to obtain $(\nabla \mathbf{u})_{\text{SH}}$, therefore to transform $(\nabla \mathbf{u}^*)_{\text{SH}}$ in the laboratory frame of reference, the following matrix operation should be performed:

$$(\nabla \mathbf{u})_{\text{SH}} = \mathbf{Q}^T [(\nabla \mathbf{u}^*)_{\text{SH}}] \mathbf{Q}.$$

From the obtained shear component of the velocity gradient tensor, the vorticity associated to the shear contribution ω_{SH} was calculated.

APPENDIX B: SENSITIVITY OF THE THICKNESS OF THE INTERNAL LAYERS OF INTENSE SHEAR TO THE CONSTANTS OF THE IDENTIFICATION METHODS

This Appendix is meant to examine how variations of the constants for the identification of the internal layers of intense shear (K and C in Sec. II) affect the thickness of the bespoke layers. First, we focus on the mixing layer, and, second, on the jet. Figure 20(a) shows the thickness of the internal layers of intense shear, which is estimated after identifying these layers with different values of the constant K in Eq. (2). These values of the thickness are obtained from conditionally averaged velocity profiles characterized by positive values of $\frac{du}{dy}|_{\text{IL}}$, where the local velocity of the points of the internal layers is in the range $0.25 < (\Delta U - u_i)/u_{\text{rms}} < 0.50$. As can be observed, the thickness of the internal layers is rather insensitive to the constant K in Eq. (2) (Sec. II). Therefore, because the intensity of the internal layers does not affect significantly their thickness, it was decided to consider a constant of $K = 1.5$ in Eq. (2) for most of the analysis presented in Sec. III.

If we move to examine the jet, we can observe that analogous conclusions can be drawn. In Fig. 20(b), the thickness of the internal layers of intense shear is presented, which is estimated for different values of the constant C in Eq. (4), both for the jet with circular orifice as well as with the jet with fractal orifice. These values of the thickness are obtained from conditionally averaged

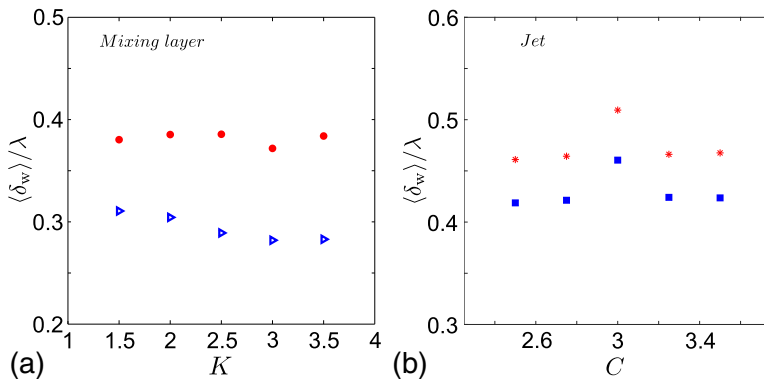


FIG. 20. (a) Thickness of the internal layers of intense shear identified in the mixing layer at different values of the constant K in Eq. (2), within the range $0.25 < (\Delta U - u_i)/u_{\text{rms}} < 0.50$. Only the profiles characterized by positive values of $\frac{du}{dy}|_{\text{IL}}$ are retained and contribute to the averages. Red full \bullet symbols refer to $Re_\lambda \approx 200$, while blue empty \triangleright symbols refer to $Re_\lambda \approx 275$. (b) Thickness of the internal layers of intense shear identified in the jet at different values of the constant C in Eq. (4). Only the profiles characterized by positive values of $\frac{du}{dy}|_{\text{IL}}$ are retained and contribute to the averages. Blue full \square symbols refer to the jet with circular orifice, while red asterisks $*$ refer to the jet with fractal orifice.

velocity profiles characterized by positive values of $\frac{du}{dy}|_{\text{IL}}$. The thickness of the internal layers is not particularly sensitive to variations of the constant C in Eq. (4). Moreover, the observed deviations from the thickness obtained for $C = 3$, which was adopted in the analysis reported in Sec. IV, do not appear to question the scaling law $\langle \delta_w \rangle / \lambda \sim Re_\lambda^{-1/2}$, indicating a Kolmogorov scaling for these internal layers.

APPENDIX C: SENSITIVITY OF THE CONDITIONALLY AVERAGED PROFILES OF STREAMWISE VELOCITY TO THE CONSTANTS OF THE IDENTIFICATION METHODS

This Appendix shows the sensitivity of the conditionally averaged profiles of streamwise velocity to variations of the constants for the identification of the internal layers of intense shear K and C , respectively, for the jet and for the mixing layer. First, we consider the profiles of streamwise velocities characterized by positive values of $\frac{du}{dy}|_{\text{IL}}$. These are presented in Figs. 21 and 22,

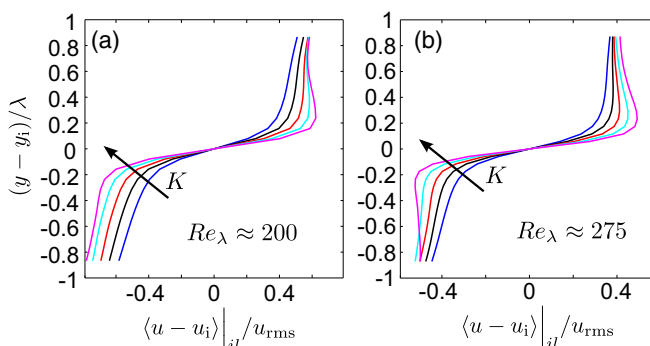


FIG. 21. Conditionally averaged profiles of streamwise velocity identified in the mixing layer in the vicinity of internal layers of intense shear, at different values of the constant K in Eq. (2), within the range $0.25 < (\Delta U - u_i)/u_{\text{rms}} < 0.50$, at (a) $Re_\lambda \approx 200$ and (b) $Re_\lambda \approx 275$. Only the profiles characterized by positive values of $\frac{du}{dy}|_{\text{IL}}$ are retained and contribute to the averages.

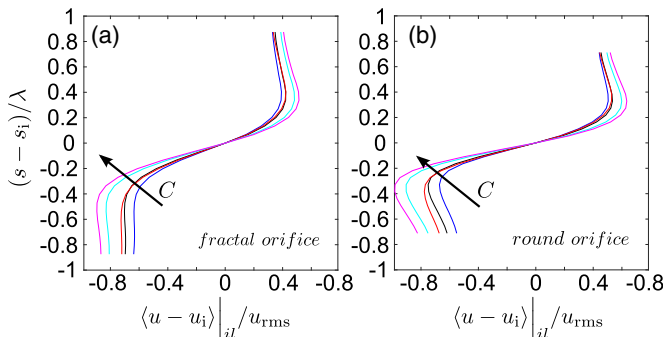


FIG. 22. Conditionally averaged profiles of the streamwise velocity in the near vicinity of the internal layers of intense shear, at different values of the constant C in Eq. (4), for (a) the jet with fractal orifice and (b) the jet with round orifice. Only the profiles characterized by positive values of $\frac{du}{dy}|_{IL}$ are retained and contribute to the calculation.

respectively, for the mixing layer and for the jet. As can be observed, variations of the constant K do not affect the shape of these profiles. Increasing values of K and of C are associated with more intense events, which results in mildly larger velocity jumps across the internal layers of intense shear. This trend can be found from the analysis of both the mixing layer and the jet.

Analogous to these observations for positive values of $\frac{du}{dy}|_{IL}$, negative values of $\frac{du}{dy}|_{IL}$ lead to velocity profiles that are not significantly altered by variations of the constants K and C . Growing of K and of C is associated with more intense events, which result in mildly larger velocity jumps across the internal layers of intense shear, as presented in Figs. 23 and 24.

APPENDIX D: SENSITIVITY OF THE CONDITIONAL TOPOLOGICAL CONTENT TO THE CONSTANTS OF THE IDENTIFICATION METHODS

In this Appendix, we examine how variations of the constant for the identification of the internal layers of intense shear [K in Eq. (2)] and for the identification of the internal layers of intense SG [H in Eq. (5)] affect the joint probability density functions of the second (Q) and third (R) invariants of the velocity gradient tensor presented in Figs. 17(b) and 17(c). Figures 25(a) and 25(b) show the JPDF of Q and R in points of intense scalar gradient, identified after setting $H = 0.4$

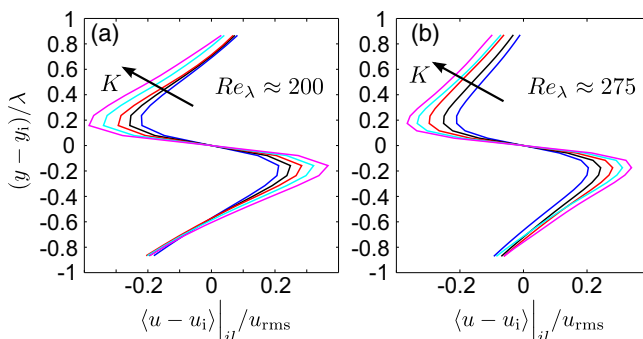


FIG. 23. Conditionally averaged profiles of streamwise velocity identified in the mixing layer in the vicinity of internal layers of intense shear, at different values of the constant K in Eq. (2), within the range $0.25 < (\Delta U - u_i)/u_{rms} < 0.50$, at (a) $Re_\lambda \approx 200$ and (b) $Re_\lambda \approx 275$. Only the profiles characterized by negative values of $\frac{du}{dy}|_{IL}$ are retained and contribute to the averages.

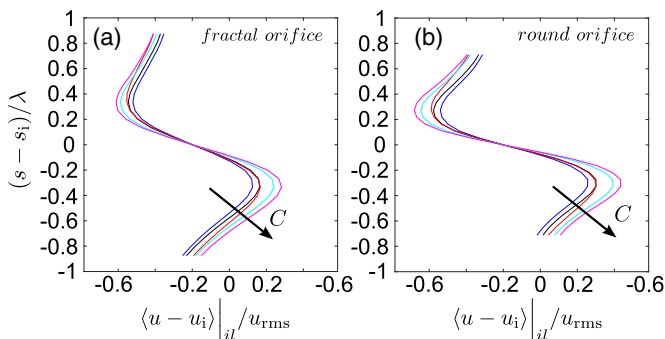


FIG. 24. Conditionally averaged profiles of the streamwise velocity in the near vicinity of the internal layers of intense shear, at different values of the constant C in Eq. (4), for (a) the jet with fractal orifice and (b) the jet with round orifice. Only the profiles characterized by negative values of $\frac{du}{dy}|_{IL}$ are retained and contribute to the calculation.

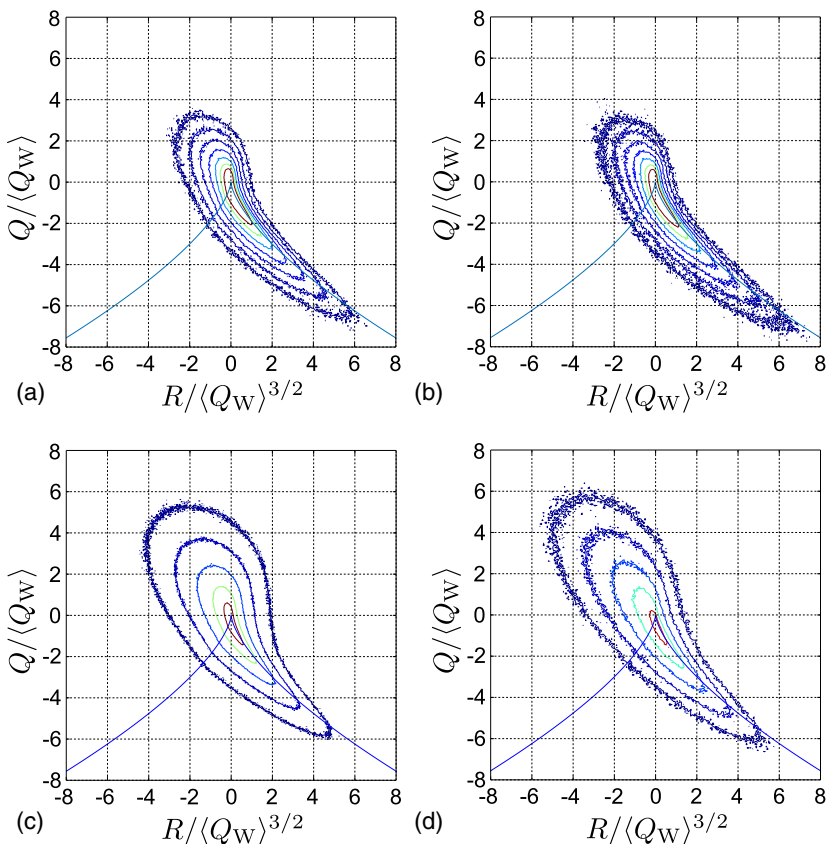


FIG. 25. Joint probability density functions of the second (Q) and third (R) invariants of the velocity gradient tensor (a) in points of intense scalar gradient with $H = 0.4$ in Eq. (5), (b) in points of intense scalar gradient with $H = 0.5$ in Eq. (5), (c) in points of intense shear vorticity with $K = 2$ at $\text{Re}_\lambda \approx 200$, (d) in points of intense shear vorticity with $K = 3$ at $\text{Re}_\lambda \approx 275$. The regions within the different JPDFs are described in the caption of Fig. 17. $Q_W = (\nabla \times \mathbf{u})^2/4$.

and 0.5 in Eq. (5), respectively. As can be observed, the differences between these JPDFs and the JPDF reported in Fig. 17(c), and obtained after setting $H = 0.6$, are modest. Overall, it appears that the JPDF calculated in points of increasingly more intense scalar gradient exhibits a longer tail, which results in a growing dominance of the node/saddle/saddle topology. The percentage of points characterized by a node/saddle/saddle topology is 52, 56, and 59% when setting the value of the H coefficient in Eq. (5) to $H = 0.4, 0.5$, and 0.6 , respectively. Nonetheless, varying the coefficient H does not affect significantly the results, and, even though less pronounced, a dominance of the node/saddle/saddle topology can still be found.

The same observations can be made when calculating the JPDF of Q and R in points of intense shear, after setting $K = 2$ in Eq. (2). When comparing Fig. 25(c) with Fig. 17(b), which is obtained for $K = 2.5$, it can be seen that the JPDFs are similar, even though the JPDF obtained considering events at higher intensity, in Fig. 17(b), tends to be more skewed towards region I, associated with a more pronounced dominance of stable focus/stretching. This trend can also be observed when examining Fig. 25(d), which is obtained for $K = 3$. Regardless, the results are not importantly affected by the value of K .

-
- [1] S. Corrsin and A. Kistler, Free-stream boundaries of turbulent flows, NASA Technical Report No. **1244**, 1955 (unpublished).
 - [2] D. Bisset, J. Hunt, and M. Rogers, The turbulent/non-turbulent interface bounding a far wake, *J. Fluid Mech.* **451**, 383 (2002).
 - [3] J. Westerweel, C. Fukushima, J. M. Pedersen, and J. C. R. Hunt, Mechanics of the Turbulent-Nonturbulent Interface of a Jet, *Phys. Rev. Lett.* **95**, 174501 (2005).
 - [4] J. Westerweel, C. Fukushima, J. Pedersen, and J. Hunt, Momentum and scalar transport at the turbulent/non-turbulent interface of a jet, *J. Fluid Mech.* **631**, 199 (2009).
 - [5] M. Gampert, V. Narayanaswamy, P. Schaefer, and N. Peters, Conditional statistics of the turbulent/non-turbulent interface in a jet flow, *J. Fluid Mech.* **731**, 615 (2013).
 - [6] M. Gampert, J. Boschung, F. Hennig, M. Gauding, and N. Peters, The vorticity versus the scalar criterion for the detection of the turbulent/non-turbulent interface, *J. Fluid Mech.* **750**, 578 (2014).
 - [7] M. van Reeuwijk and M. Holzner, The turbulence boundary of a temporal jet, *J. Fluid Mech.* **739**, 254 (2014).
 - [8] A. Attili, J. Cristancho, and F. Bisetti, Statistics of the turbulent/non-turbulent interface in a spatially developing mixing layer, *J. Turbul.* **15**, 555 (2014).
 - [9] K. Chauhan, J. Philip, C. de Silva, N. Hutchins, and I. Marusic, The turbulent/non-turbulent interface and entrainment in a boundary layer, *J. Fluid Mech.* **741**, 119 (2014).
 - [10] K. Chauhan, J. Philip, and I. Marusic, Scaling of the turbulent/non-turbulent interface in boundary layers, *J. Fluid Mech.* **751**, 298 (2014).
 - [11] D. Borrell and J. Jiménez, Properties of the turbulent/non-turbulent interface in boundary layers, *J. Fluid Mech.* **801**, 554 (2016).
 - [12] T. Silva, M. Zecchetto, and C. da Silva, The scaling of the turbulent/non-turbulent interface at high Reynolds numbers, *J. Fluid Mech.* **843**, 156 (2018).
 - [13] T. Watanabe, C. da Silva, Y. Sakai, K. Nagata, and T. Hayase, Lagrangian properties of the entrainment across turbulent/non-turbulent interface layers, *Phys. Fluids* **28**, 031701 (2016).
 - [14] T. Watanabe, C. da Silva, K. Nagata, and Y. Sakai, Geometrical aspects of turbulent/non-turbulent interfaces with and without mean shear, *Phys. Fluids* **29**, 085105 (2017).
 - [15] D. Mistry, J. Philip, J. Dawson, and I. Marusic, Entrainment at multi-scales across the turbulent/non-turbulent interface in an axisymmetric jet, *J. Fluid Mech.* **802**, 690 (2016).
 - [16] J. Eisma, J. Westerweel, G. Ooms, and G. Elsinga, Interfaces and internal layers in a turbulent boundary layer, *Phys. Fluids* **27**, 055103 (2015).

- [17] C. de Silva, J. Philip, N. Hutchins, and I. Marusic, Interfaces of uniform momentum zones in turbulent boundary layers, *J. Fluid Mech.* **820**, 451 (2017).
- [18] D. Fan, J. Xu, M. Yao, and J. Hickey, On the detection of internal interfacial layers in turbulent flows, *J. Fluid Mech.* **872**, 198 (2019).
- [19] M. Gul, G. Elsinga, and J. Westerweel, Internal shear layers and edges of uniform momentum zones in a turbulent pipe flow, *J. Fluid Mech.* **901**, A10 (2020).
- [20] G. Elsinga, T. Ishihara, M. Goudar, and C. da Silva, The scaling of straining motions in homogeneous isotropic turbulence, *J. Fluid Mech.* **829**, 31 (2017).
- [21] T. Ishihara, Y. Kaneda, and J. Hunt, Thin shear layers in high Reynolds number turbulence: DNS results, *Flow Turbul. Combust.* **91**, 895 (2013).
- [22] J. C. R. Hunt, T. Ishihara, N. A. Worth, and Y. Kaneda, Thin shear layer structures in high Reynolds number turbulence, *Flow Turbul. Combust.* **92**, 607 (2014).
- [23] G. Elsinga and I. Marusic, Universal aspects of small-scale motions in turbulence, *J. Fluid Mech.* **662**, 514 (2010).
- [24] G. Elsinga and C. da Silva, How the turbulent/non-turbulent interface is different from internal turbulence, *J. Fluid Mech.* **866**, 216 (2019).
- [25] G. Brethouwer, J. Hunt, and F. Nieuwstadt, Micro-structure and lagrangian statistics of the scalar field with a mean gradient in isotropic turbulence, *J. Fluid Mech.* **474**, 193 (2003).
- [26] A. Attili and F. Bisetti, Statistics and scaling of turbulence in a spatially developing mixing layer at $Re_\lambda = 250$, *Phys. Fluids* **24**, 035109 (2012).
- [27] A. Attili and F. Bisetti, Fluctuations of a passive scalar in a turbulent mixing layer, *Phys. Rev. E* **88**, 033013 (2013).
- [28] D. Fiscaletti, A. Attili, F. Bisetti, and G. E. Elsinga, Scale interactions in a mixing layer: The role of the large-scale gradients, *J. Fluid Mech.* **791**, 154 (2016).
- [29] D. Fiscaletti, G. E. Elsinga, A. Attili, F. Bisetti, and O. R. H. Buxton, Scale dependence of the alignment between strain rate and rotation in turbulent shear flow, *Phys. Rev. Fluids* **1**, 064405 (2016).
- [30] V. Kolář, Vortex identification: New requirements and limitations, *Int. J. Heat Fluid Flow* **28**, 638 (2007).
- [31] R. Nagata, T. Watanabe, K. Nagata, and C. da Silva, Triple decomposition of velocity gradient tensor in homogeneous isotropic turbulence, *Comput. Fluids* **198**, 104389 (2020).
- [32] R. Taveira and C. da Silva, Kinetic energy budgets near the turbulent/nonturbulent interface in jets, *Phys. Fluids* **25**, 015114 (2013).
- [33] M. Breda and O. Buxton, Effects of multiscale geometry on the large-scale coherent structures of an axisymmetric turbulent jet, *J. Visualization* **21**, 525 (2018).
- [34] M. Breda and O. Buxton, Influence of coherent structures on the evolution of an axisymmetric turbulent jet, *Phys. Fluids* **30**, 035109 (2018).
- [35] N. Worth, T. Nickels, and N. Swaminathan, A tomographic PIV resolution study based on homogeneous isotropic turbulence DNS data, *Exp. Fluids* **49**, 637 (2010).
- [36] O. Buxton, S. Laizet, and B. Ganapathisubramani, The effects of resolution and noise on kinematic features of fine-scale turbulence, *Exp. Fluids* **51**, 1417 (2011).
- [37] M. Breda, Influence of coherent structures on the near- and far-field evolution of an axisymmetric turbulent jet, Ph.D. dissertation, Massimiliano Breda, Imperial College (2018).
- [38] M. Breda and O. Buxton, Behaviour of small-scale turbulence in the turbulent/non-turbulent interface region developing turbulent jets, *J. Fluid Mech.* **879**, 187 (2019).
- [39] S. Tokgöz, G. E. Elsinga, R. Delfos, and J. Westerweel, Spatial resolution and dissipation rate estimation in Taylor–Couette flow from tomographic PIV, *Exp. Fluids* **53**, 561 (2012).
- [40] J. Mathew and A. J. Basu, Some characteristics of entrainment at a cylindrical turbulent boundary, *Phys. Fluids* **14**, 2065 (2002).
- [41] C. B. da Silva and J. F. C. Pereira, Invariants of the velocity-gradient, rate-of-strain, and rate-of-rotation tensors across the turbulent/nonturbulent interface in jets, *Phys. Fluids* **20**, 055101 (2008).
- [42] W. Gander, G. H. Golub, and R. Strebler, Least-squares fitting of circles and ellipses, *BIT Num. Math.* **34**, 558 (1994).
- [43] S. Pope, *Turbulent Flows* (Cambridge University Press, Cambridge, England, 2000).

- [44] O. Buxton, R. de Kat, and B. Ganapathisubramani, The convection of large and intermediate scale fluctuations in a turbulent mixing layer, *Phys. Fluids* **25**, 125105 (2013).
- [45] O. Buxton and B. Ganapathisubramani, Concurrent scale interactions in the far-field of a turbulent mixing layer, *Phys. Fluids* **26**, 125106 (2014).
- [46] L. Wei, G. Elsinga, G. Brethouwer, P. Schlatter, and A. Johansson, Universality and scaling phenomenology of small-scale turbulence in wall-bounded flows, *Phys. Fluids* **26**, 035107 (2014).
- [47] G. Brown and A. Roshko, On density effects and large structure in turbulent mixing layers, *J. Fluid Mech.* **64**, 775 (1974).
- [48] J. Jiménez, A. Wray, P. Saffman, and R. S. Rogallo, The structure of intense vorticity in isotropic turbulence, *J. Fluid Mech.* **225**, 65 (1993).
- [49] B. Ganapathisubramani, K. Lakshminarasimhan, and N. Clemens, Investigation of three-dimensional structure of fine scales in a turbulent jet by using cinematographic stereoscopic particle image velocimetry, *J. Fluid Mech.* **598**, 141 (2008).
- [50] D. Fiscaletti, J. Westerweel, and G. Elsinga, Long-range μ PIV to resolve the small scales in a jet at high Reynolds number, *Exp. Fluids* **55**, 1812 (2014).
- [51] D. Carter and F. Coletti, Small-scale structure and energy transfer in homogeneous turbulence, *J. Fluid Mech.* **854**, 505 (2018).
- [52] G. Xu and R. Antonia, Effect of different initial conditions on a turbulent round free jet, *Exp. Fluids* **33**, 677 (2002).
- [53] T. Watanabe, K. Tanaka, and K. Nagata, Characteristics of shearing motions in incompressible isotropic turbulence, *Phys. Rev. Fluids* **5**, 072601(R) (2020).
- [54] M. Holzner and B. Lüthi, Laminar Superlayer at the Turbulence Boundary, *Phys. Rev. Lett.* **106**, 134503 (2011).
- [55] M. Chong, A. Perry, and B. Cantwell, A general classification of three-dimensional flow fields, *Phys. Fluids A* **2**, 765 (1990).
- [56] A. Ooi, J. Martin, J. Soria, and M. Chong, A study of the evolution and characteristics of the invariants of the velocity-gradient tensor in isotropic turbulence, *J. Fluid Mech.* **381**, 141 (1999).
- [57] G. Elsinga and I. Marusic, Evolution and lifetimes of flow topology in a turbulent boundary layer, *Phys. Fluids* **22**, 015102 (2010).
- [58] J. Soria, R. Sondergaard, B. Cantwell, M. Chong, and A. E. Perry, A study of the fine-scale motions of incompressible time-developing mixing layers, *Phys. Fluids* **6**, 871 (1994).
- [59] H. Blackburn, N. Mansour, and B. Cantwell, Topology of fine-scale motions in turbulent channel flow, *J. Fluid Mech.* **310**, 269 (1996).
- [60] M. Chong, J. Soria, A. Perry, J. Chacin, B. Cantwell, and Y. Na, A study of the turbulence structures of wall-bounded shear flows using DNS data, *J. Fluid Mech.* **357**, 225 (1998).
- [61] C. da Silva, J. Hunt, I. Eames, and J. Westerweel, Interfacial layers between regions of different turbulence intensity, *Annu. Rev. Fluid Mech.* **46**, 567 (2014).
- [62] R. Taveira and C. da Silva, Characteristics of the viscous superlayer in shear free turbulence and in planar turbulent jets, *Phys. Fluids* **26**, 021702 (2014).
- [63] W. van de Water, J. Eisma, J. Westerweel, and D. Tam, What makes the boundary of uniform concentration zones? in Proceedings of the 71st Annual Meeting of the APS Division of Fluid Dynamics, 2018 (unpublished).
- [64] T. Silva and C. da Silva, The behaviour of the scalar gradient across the turbulent/non-turbulent interface in jets, *Phys. Fluids* **29**, 085106 (2017).